

**Title page**

**Spinodal decomposition in a melt-spun Cu-15Ni-8Sn alloy**

Shin-ichiro Kondo\*, Hiromichi Nakashima, Takao Morimura

Department of Materials Science and Engineering, Faculty of Engineering, Nagasaki  
University, Nagasaki 852-8521, Japan

**\*Corresponding author:** Shin-ichiro Kondo

Department of Materials Science and Engineering, Faculty of Engineering, Nagasaki  
University, 1-14 Bunkyo-machi, Nagasaki 852-8521, Japan

Tel.: +81-95-819-2635; Fax: +81-95-819-2635; E-mail: kondou@nagasaki-u.ac.jp

## **Abstract**

We investigate the spinodal decomposition process in a melt-spun Cu-15Ni-8Sn alloy using X-ray diffraction (XRD), transmission electron microscopy (TEM), and electron diffraction analyses. In the XRD measurements, an aging treatment of more than 300 min at 350 °C was required to obtain the (200) sidebands. TEM observations of the melt-spun samples aged at 350 °C for 40, 60, and 300 min showed a modulated structure with a wavelength too small to be detected by TEM and aging for about 1200 min was required for the clear appearance of a modulated structure. The electron diffraction patterns showed only the disordered fcc phase with no satellite structures in the sample aged for 20 min at 350 °C, which implied that no spinodal decomposition occurred. Aging for 40 min at 350 °C was required before the super-lattice reflection of DO<sub>22</sub> was observed. These experimental results indicate that the decomposition process in the melt-spun alloy was slow initially.

**Keywords:** melt-spun; sideband; satellite; Cu-Ni-Sn alloy; superlattice reflection; spinodal decomposition

## 1. Introduction

The commercial Cu-Ni-Sn alloy, C72900 ASTM B740-84, which was developed by Bell Laboratories in the 1970s as a substitute for potentially hazardous Cu-Be alloys[1-3], has wide industrial applications in bushings, bearings, springs, and electronic connectors [4,5]. Extensive X-ray diffraction (XRD) [6-9], transmission electron microscopy (TEM) [9-12], and X-ray small-angle scattering (XSAS) [13] studies have shown that Cu-15Ni-8Sn and related alloys exhibit spinodal decomposition, and show a characteristic modulated structure with Sn-rich and Sn-lean zones during the early stage of aging [10-12,14].

Based on the time-temperature-transformation (TTT) diagram for this alloy, obtained by TEM and electrical resistivity measurements [12], at temperatures above 550 °C, a discontinuous  $\gamma(\text{DO}_3)$  phase precipitates without spinodal decomposition from an  $\alpha$  phase. At temperatures between 550 and 300 °C, spinodal decomposition initially occurs without ordering, and then with  $\text{DO}_{22}$  ordering as the annealing time is increased. This  $\text{DO}_{22}$  ordering phase, the crystalline structure of which is the same as that of intermetallic compounds  $\text{Al}_3\text{Ti}$  or  $\text{Ni}_3\text{V}$ , has an ordered tetragonal  $(\text{Cu}_x\text{Ni}_{1-x})_3\text{Sn}$  structure with  $a = 0.377$  nm and  $c = 0.724$  nm. The  $\text{DO}_{22}$  phase precipitates with a needle-like shape, generating various strain fields in the matrix. Upon further annealing,  $\text{L}_{12}$  ordering appears. This has the same crystalline  $(\text{Cu}_x\text{Ni}_{1-x})_3\text{Sn}$  structure as  $\text{AuCu}_3$ . The  $\text{L}_{12}$  phase nucleates at the  $\text{DO}_{22}/\text{fcc}$  interface with a spherical or cuboidal shape, relaxing the strain fields in the matrix. Finally, the mixed  $\text{L}_{12} + \text{DO}_{22}$  phase structures become dominant. At temperatures below 300 °C, spinodal decomposition occurs first and then mixed phases of  $\text{L}_{12} + \text{DO}_{22}$  structures simultaneously appear afterward.

However, the kinetic mechanism of this alloy is not completely understood.

Divergent conclusions about the spinodal decomposition of this alloy have been reported, including that spinodal decomposition occurs prior to ordering [11-12,14-16] or during quenching [10,17], and that there is no relation between hardening and spinodal decomposition [13,18]. These different explanations arise from the uncertainty about the role of the initial state.

In our previous work [9], therefore, we focused on the kinetic mechanism, particularly in the initial state before annealing, because the initial state determines the subsequent spinodal decomposition processes. During spinodal decomposition, clustering is an essential step in the spontaneous separation of a homogeneous, supersaturated solid solution into two phases, each with the same crystal structure but different compositions. Spinodal decomposition, especially in its early stage, is initiated by concentration fluctuations. Small concentration fluctuations in a supersaturated solid solution can be easily enhanced by annealing, eventually resulting in macroscopic phase separation. Thus, small clusters can trigger spinodal decomposition.

After solutionizing heat treatment, which is usually performed prior to aging, the sample is rapidly cooled from a high temperature by quenching in cold water. This produces a homogeneous, supersaturated solid solution that retains its high-temperature atomic arrangements and other thermodynamically unstable states. For quenching in iced water, the cooling rate can be as low as  $10^3$  °C/s; thus, small clusters formed by high-temperature atomic arrangements may exist. In contrast, when sample is fabricated by melt-spinning, it is unlikely that small clusters remain because of the high cooling rate of  $8 \times 10^5$  °C/s [19]. Accordingly, the difference in cooling rate may affect the subsequent spinodal decomposition processes. For example, in the Cu-Ti alloys, experimental results suggest that spinodal decomposition may be involved in the

formation of the coherent  $\text{Cu}_4\text{Ti}$  ( $\text{D1}_a$ ) precipitate phase [20], whereas ordering appears to follow clustering in the Ti-enriched regions in melt-spun Cu-Ti alloys [21].

In previous work [9], based on comparing different cooling rates ( $1 \times 10^3$  and  $8 \times 10^5$  °C/s), we concluded that the early stage spinodal decomposition is strongly affected by the initial state. In the quenched sample fabricated by the conventional method (cooling rate of about  $1 \times 10^3$  °C/s), the spinodal decomposition process was faster than that in the melt-spun sample, probably due to the presence of small clusters formed by this relatively low cooling rate. However, we have not fully examined the as-quenched (AS-Q) state and the early stages of spinodal decomposition, which are connected by the initial states. We did not obtain electron diffraction patterns of the As-Q melt-spun samples and samples annealed for 20 and 40 min in the previous work [9]. Consequently, detailed investigation of the early stages of decomposition is necessary to confirm the conclusion of our previous work [9], that the spinodal decomposition is slow in the case of melt-spun samples. Furthermore, longer annealing times of 300 and 1200 min were not examined, and thus the results were insufficient for discussing the whole decomposition process of the alloy.

In the present work, we confirm the conclusions of our previous work [9] and investigate the details of the spinodal decomposition of a melt-spun alloy by examining the whole spinodal decomposition process (from the As-Q state to 1200 min annealing). We use electron diffraction, bright-field (BF), and dark-field (DF) images to analyze samples after each annealing time. Furthermore, we compare our experimental results with those of Zhao and Notis [12], who analyzed quenched samples fabricated by the conventional method.

## 2. Experimental

Small pieces of oxygen-free copper (99.99%), nickel (99.99%), and tin (99.99%) were placed in a high-frequency furnace at a weight ratio of Cu-15 wt.% Ni-8 wt.% Sn and melted together under argon gas shielding to obtain the ingot.

Melt-spun specimens were fabricated under an argon gas atmosphere using a single-roller melt-spinning apparatus. The melt-spun samples (3 g) were quenched from the melted ingot at about 1250 °C, a surface velocity of 42 m/s, and a blow-off pressure of 0.6 atm. The melt-spun samples were 50–60 µm thick, 1–1.5 mm wide, and they were aged at 350 °C for 0 (As-Q), 20, 40, 60, 300, 600, and 1200 min.

XRD analysis with a Cu-K $\alpha$  radiation source was conducted to investigate sidebands and new ordered phases that formed during aging. In particular, to detect the sidebands of (200) planes, step scanning was performed from 47° to 53° at a scanning speed of 0.3°/min, based on the scanning speed of 0.25°/min reported by Findik [22].

For TEM, we selected melt-spun samples that were As-Q and aged at 350 °C for 20, 40, 60, 300, and 1200 min to identify structural differences and clarify the progress of spinodal decomposition. Discs for TEM (diameter of about 3 mm) were punched from the samples and polished by ion milling. High-resolution TEM (JEM2010, JEOL) at 200 kV was used to observe the microstructures and conduct selected-area diffraction pattern (SADP) analysis. In the SADP measurements with a CCD camera, we used an exposure time of 0.1 s for satellite structures and 1.0 s for super-lattice reflections. As reported by Zhao and Notis [12], SADP depends on exposure time. A short exposure time is used for measuring spinodal satellites because the bright fundamental reflections obtained with a long exposure time wash out the satellites. In contrast, a long exposure time is required to observe super-lattice reflections.

### 3. Results and discussion

#### 3.1. XRD measurements

Figure 1 shows XRD measurements from  $20^\circ$  to  $80^\circ$  for the melt-spun sample aged at  $350^\circ\text{C}$ . For 1200 min aging,  $\delta$  (002) and  $\delta$  (121) peaks attributed to the appearance of the  $\delta$  phase, which is an equilibrium precipitate in addition to  $\alpha$  and  $\gamma(\text{DO}_3)$  phases [18,23,24], were observed around the Cu (111) peak. However, in this study, there were no  $\gamma$  (400), (122), and (202) peaks around  $2\theta = 60^\circ$  related to precipitation of the  $\gamma(\text{DO}_3)$  phase.

The relative intensities of the Cu (111) and (200) peaks are shown in Table 1, where we set the intensity of the Cu (111) peak as 1. The relative intensities of the peaks decreased with annealing time. Based on the theoretical analysis of pure Cu powder, the relative intensity of the Cu (200) peak was calculated as 0.45 by same method. The measured relative intensity of the Cu (200) peak was about twice as large as the calculated value in the early stages (As-Q to 40 min annealing). This result indicates that the Cu (200) phase appeared readily when the cooling rate was large ( $8 \times 10^5^\circ\text{C/s}$ ). The decrease in the relative intensity of the (200) peak arose from the rearrangement of the crystal grains during annealing, probably via the recovery process.

Lattice parameter  $a$  for the annealed samples, determined by RIETAN-FP [25], is given in Table 2. The change in  $a$  was small, irrespective of annealing time, indicating that annealing had little effect on  $a$ . The precipitation of the  $\text{DO}_{22}$  phase increases the lattice parameter, whereas that of the  $\text{L}_{12}$  phase decreases the lattice extension. The experimental results shown in Table 2 suggest that the coexistence of both phases cancelled out the change in  $a$ .

The step scanning results of the (200) diffraction profiles from  $47^\circ$  to  $53^\circ$  for the

same samples are shown in Fig. 2. The appearance of sidebands is shown in the enlarged views around the Cu (200) peak in Fig. 2(a)–(d). An annealing time of more than 300 min was required to produce the sideband (Fig. 2(c)). In our previous work, distinct sidebands were visible in the quenched sample aged at 350 °C for 60 min [9]; thus, the present experimental result may suggest that the decomposition process was slow when samples were fabricated with a single-roller melt-spinning apparatus.

For the melt-spun samples aged at 350 °C, we evaluated the wavelength,  $\lambda$ , of the spinodal decomposition with the Daniel-Lipson formula [26-28]

$$\lambda = a_0 \frac{h \tan \theta}{(h^2 + k^2 + l^2) \delta \theta} \quad (1)$$

where  $\theta$  is the Bragg angle of the fundamental cubic peak,  $\delta \theta$  is the distance of the angle between the side-band and the Bragg peak,  $a_0$  is a lattice parameter of the matrix alloy in its initial state before spinodal decomposition, and  $h$ ,  $k$ , and  $l$  are the Miller indices of the Bragg peak ( $h = 2$  and  $k = l = 0$ ). From eq. (1), we obtain  $\lambda \approx 5$  and 8 nm for the melt-spun samples with aging times of 300 and 1200 min. Consequently, the increase in the wavelength caused by annealing indicates the progression of spinodal decomposition.

### 3.2 TEM observations and electron diffraction

We examined the microstructure of the alloy by TEM and electron diffraction. To identify the super-lattice reflections, the diffraction patterns of the fcc matrix, DO<sub>22</sub>, and L1<sub>2</sub> ordering reflections reported by Zhao and Notis [12] are given in Fig. 3.

Figure 4(a) shows the TEM BF images of the As-Q melt-spun sample. The images contained no modulated structures, which are characteristic of spinodal decomposition.



The DF image of the As-Q melt-spun sample is shown in Fig. 4(b). Similar to Fig. 4(a), no modulated structures were observed. However, the edge of the sample was bright compared with other areas, which was probably caused by stress. Figure 4(c) shows the SADP of the As-Q melt-spun sample (exposure time 0.1 s). No satellite structures were observed, indicating the presence of the disordered fcc phase ( $\alpha$  phase). Additionally no super-lattice reflections were observed, even for an exposure time of 1.0 s.

Figure 5(a) shows the TEM BF images of the melt-spun sample annealed for 20 min at 350 °C, and an enlarged view is given in Fig. 5(a'). No distinct modulated structures were observed. The DF image of the same sample showed no modulated structures (Fig. 5(b)). Figure 5(c) shows the SADP of the same sample with no super-lattice reflections even for an exposure time of 1.0 s. No satellite structures were observed for an exposure time of 0.1 s. Based on the results in Fig. 5(a), (a'), (b), and (c), we concluded that the disordered fcc phase ( $\alpha$  phase) was dominant after annealing for 20 min at 350 °C. Although no modulated structures were observed in Fig. 5(a') and (b), a trace amount of the modulated structures may exist.

Figure 6(a) shows TEM BF images of the melt-spun sample annealed for 40 min at 350 °C, and an enlarged view is given in Fig. 6(a'). The enlarged image shows a modulated structure; however, it is unclear because  $\lambda$  was too small to measure. The DF image of the same sample is shown in Fig. 6(b). Similar to the BF images, no modulated structures were observed, even in the magnified image. SADPs of the same sample are shown in Fig. 6(c) (exposure time 0.1 s) and (d) (exposure time 1.0 s). The  $(0\ 2\bar{2})$  reflection exhibited satellite structures (insets in Fig. 6(c)), which indicated concentration fluctuation caused by spinodal decomposition. The  $\{0\ 1/2\ 1\}$  spot originating from DO<sub>22</sub> ordering was observed (Fig. 6(d)), although the image was

unclear. These results suggest that both spinodal decomposition and the precipitation of DO<sub>22</sub> phase occurred.

Figure 7(a) shows the TEM BF images of the melt-spun sample annealed for 60 min at 350 °C, and an enlarged view is given in Fig. 7(a'). The modulated structure is clearer compared with Fig. 6(a'), although it is still unclear because  $\lambda$  was too small. We did not expect this structure to show sidebands. However, assuming that the slight increase in XRD intensity from 47° to 48° (Fig. 2(b)) was from the sideband,  $\lambda$  was estimated to be 3.1 nm from eq. (1), which was too small to be detected by TEM BF. The DF image of same sample is shown in Fig. 7(b) and an enlarged view is given in Fig. 7(b'). In contrast to the BF image, the modulated structure was clearer, and we estimated that  $\lambda$  was less than 5 nm. SADPs of the same sample are shown in Fig. 7(c) (exposure time 0.1 s) and (d) (exposure time 1.0 s). The (002), (0 $\bar{2}$ 0), and (0 $\bar{2}$ 2) reflections had satellite structures, implying concentration fluctuation. In Fig. 7(d), the {0 1/2 1} spot originating from DO<sub>22</sub> ordering was clear compared with Fig. 6(d). These experimental results suggest the presence of the DO<sub>22</sub> phase and spinodal decomposition in the sample annealed for 60 min at 350 °C.

Figure 8(a) shows the TEM BF micrographs of the melt-spun sample aged at 350 °C for 300 min. This image showed a modulated structure characteristic of spinodal decomposition. However, the modulated structure was unclear, because  $\lambda$  was too small to measure, indicating that  $\lambda$  was experimentally small because of the calculated value of 5 nm from eq. (1). SADPs of melt-spun samples aged at 350 °C for 300 min are shown in Fig. 8(b) (exposure time 1.0 s). As shown in the insets of Fig. 8(b), the intensity of the {0 1/2 1} spot was weak compared with that in Fig. 7(d). Based on the discussion by Zhao and Notis [12], the transformation of DO<sub>22</sub> to L1<sub>2</sub> occurs when

quenched sample is aged at 350 °C for 270 min; thus, decrease in the intensity of the  $\{0 \ 1/2 \ 1\}$  spot is caused by this transformation. Consequently, the L1<sub>2</sub> and DO<sub>22</sub> phases coexisted in the melt-spun sample aged at 350 °C for 300 min showing the transformation of DO<sub>22</sub> to L1<sub>2</sub>.

Figure 9(a) shows the TEM BF micrographs of the melt-spun sample aged at 350 °C for 1200 min, and an enlarged view is given in Fig. 9(a'). In contrast to Fig. 8(a),  $\lambda$  was clearly visible. We estimated  $\lambda$  as about 10 nm, which was consistent with the calculated value of 8 nm from eq. (1). The DF image of the same sample is shown in Fig. 9(b), and an enlarged view is given in Fig. 9(b'). The modulated structure was unclear compared with the BF images (Fig. 9(a) and (a')). The SADP of the melt-spun sample aged at 350 °C for 1200 min is shown in Fig. 9(c) (exposure time 1.0 s). As illustrated in the insets of Fig. 9(c), the  $\{0 \ 1/2 \ 1\}$  spot originating from DO<sub>22</sub> ordering is not present, and only the L1<sub>2</sub> super-lattice reflection was observed. This suggests that the DO<sub>22</sub> phase disappeared after annealing in the melt-spun sample as a result of the transformation of DO<sub>22</sub> to L1<sub>2</sub>, and the L1<sub>2</sub> phase was dominant.

### 3.3 Analysis

Based on the XRD and TEM results, the spinodal decomposition was slow in the melt-spun sample compared with the quenched samples [9,12]. For example, a sideband was clearly visible in the XRD results for the quenched sample annealed at 350 °C for 60 min [9], whereas the sideband was not detected in the melt-spun sample (Fig. 2(b)). In the melt-spun sample, the sideband took much longer (300 min) to appear (Fig. 2(c)). In the TEM BF image of specimen annealed at 350 °C for 60 min,  $\lambda$  for the melt-spun sample could not be determined owing to the fine modulated structure (Fig. 7(a)(a')),

whereas the quenched sample showed a distinct modulated structure with  $\lambda$  of 5–10 nm [9].

Based on the study by Zhao and Notis [12], SADP of the quenched sample annealed at 350 °C for 60 min showed that the  $\{001\}$  and  $\{011\}$  reflections became much stronger than the  $\{0, \frac{1}{2}, 1\}$  reflections, which indicates a transition from the DO<sub>22</sub> to L1<sub>2</sub> phase had occurred. Similar results were obtained in our previous work [9]. In melt-spun samples, this ordering diffraction pattern only appeared after 300 min (Fig. 8(b)).

Next, we discuss the differences in the XRD and TEM results between the quenched and melt-spun samples. The biggest difference was in the cooling rate, which was 10<sup>3</sup> °C/s for the quenched samples and  $8 \times 10^5$  °C/s for the melt-spun sample. The cooling rate of the melt-spun sample was 800 times faster than that of the quenched sample. Consequently, the initial conditions were greatly affected by such a huge difference in cooling rates.

As shown in Fig. 10(a), in the quenched samples, the concentration fluctuations, which are thought to form small clusters, were introduced by the solution heat treatment because the cooling rate was as low as 10<sup>3</sup>°C/s and triggered spinodal decomposition. Sagane et al. [16] reported slight concentration fluctuations formed during quenching in experiments on modulated structure evolution in Cu-Ni-Sn alloys. Consequently, we concluded that the formation process produced the distinct sidebands visible in the quenched sample aged for 60 min [9].

In contrast, the initial conditions were different in the melt-spun samples. Atom migration was assumed to be small when the samples were quenched from a liquid state by melt-spinning at a high cooling rate ( $\approx 8 \times 10^5$  °C/s). Figure 10(b) shows that there

were no clusters likely to promote spinodal decomposition in the As-Q samples. For these samples, it would take longer for the spinodal decomposition to produce a distinct sideband. Furthermore, the atomic arrangements of liquid are random compared with those of solid; thus, a high cooling rate and refrigeration of the liquid would prevent the cluster formation. Consequently, the disordered fcc phase ( $\alpha$  phase) was dominant in the melt-spun sample annealed at 350 °C for 20 min (Fig. 5(a)–(c)).

Next, we discuss the spinodal decomposition and ordering with respect to free energy. Figure 11 shows the free energy and its relationship with the disordered fcc ( $\alpha$  phase), DO<sub>22</sub>, L1<sub>2</sub>, and equilibrium precipitation of  $\gamma$ (DO<sub>3</sub>) phases, based on the work by Zhao and Notis [12]. A slight fluctuation in the composition induced by thermal energy can be easily enhanced because  $\partial^2 G / \partial c^2 < 0$ , where  $G$  and  $c$  denote the free energies of the  $\alpha$  phase and composition, respectively. At composition X (Sn-rich side), ordering occurred because the free energy of the DO<sub>22</sub> phase was lower than that of the  $\alpha$  phase. After further annealing, DO<sub>22</sub> and L1<sub>2</sub> phases coexisted at composition Y (Sn-rich side). In melt-spun samples, the decomposition rate was slow; however, no metastable phases other than the DO<sub>22</sub> and L1<sub>2</sub> phases were observed. Therefore, the free energies of the disordered fcc ( $\alpha$  phase), DO<sub>22</sub>, L1<sub>2</sub>, and equilibrium precipitation of  $\gamma$ (DO<sub>3</sub>) phases were similar to that in Fig. 11.

The free energy curve of the disordered fcc phase ( $\alpha$  phase) was concave (Fig. 11); thus, spinodal decomposition occurred first and ordering happened subsequently when the composition of the Sn-rich regions exceeded a certain value. This kinetic process is different from the model proposed by Soffa and Laughlin [29-31], which explains most cases of alloy decomposition. Based on their model, the free energy of alloys arising from congruent ordering induces spinodal decomposition with ordering first and

spinodal decomposition second.

In contrast, because the free energies of the fcc, DO<sub>22</sub>, L1<sub>2</sub>, and  $\gamma$ (DO<sub>3</sub>) phases are similar in a melt-spun sample (Fig. 11), the presence of pure spinodal decomposition, which indicates only concentration fluctuations with no ordering [12], is essential. However, we did not observe pure spinodal decomposition. From the SADPs, we estimated that the range of conditions for pure spinodal decomposition would be 20–40 min aging at 350 °C. Since the pure spinodal range in a quenched sample is narrow (about 10 s at 350 °C [12]); consequently, the detection of pure spinodal decomposition in a melt-spun sample may be challenging.

Finally, we compare our experimental results with those of Zhao and Notis [12] in Fig. 12. We determined the phases in TTT diagram using the method used by Zhao and Notis [12]. From these TTT curves, in the early stages of 20 min annealing at 350 °C, DO<sub>22</sub> and L1<sub>2</sub> phases were dominant in the quenched sample, whereas only disordered the fcc phase ( $\alpha$  phase) was present in the melt-spun sample.

In our experiments, the DO<sub>22</sub> phase was dominant after 40 min annealing (Fig. 12); however, Fig. 6(c) and (d) experimentally indicate simultaneous spinodal decomposition and appearance of the DO<sub>22</sub> phase, which seems contradictory. In the sample annealed for 40 min, the DO<sub>22</sub> phase appeared because of the increased concentration fluctuations, implying that there was no pure spinodal decomposition, and that the DO<sub>22</sub> phase was dominant. Furthermore, the DO<sub>22</sub> phase disappeared in the melt-spun sample after annealing at 350 °C for 1200 min (Fig.9(c)). On the contrary, Zhao and Notis [12] found that the DO<sub>22</sub> and L1<sub>2</sub> phases coexist in the quenched sample with the same annealing treatment. Because they determined the coexistence of the DO<sub>22</sub> and L1<sub>2</sub> phases for annealing at 350 °C for  $6 \times 10^2$  s (10 min) to  $2 \times 10^4$  s (333

min) by using TEM and electrical resistivity measurements [12], the dominant phase for an annealing time of 1200 min treatment remains unknown. However, from a thermodynamic perspective, the transformation  $\text{DO}_{22} + \text{L}_{12} \rightarrow \text{L}_{12}$  is plausible for a long annealing time, and thus the  $\text{L}_{12}$  phase would be dominant for an annealing time of 1200 min. Conclusively, the difference between the samples decreased with annealing time; thus, the difference in the initial conditions affected the early stage of spinodal decomposition.

#### 4. Conclusion

Based on the XRD (step scanning) and TEM (BF/DF imaging and SADP) results, spinodal decomposition occurred more slowly in the melt-spun samples than in the corresponding quenched sample [9,12]. This was probably due to the differences in the initial conditions arising from the fabrication method. The quenched samples showed concentration fluctuations arising from clusters, which may be formed due to the low cooling rate ( $1 \times 10^3$  °C/s) or high-temperature atomic configurations. These clusters probably promote spinodal decomposition. In contrast, the very high cooling rate ( $8 \times 10^5$  °C/s) for the melt-spun samples resulted in concentration fluctuations that were too small to promote spinodal decomposition. Therefore, longer annealing was required to induce spinodal decomposition to allow the formation and growth of clusters. For instance, an annealing time of more than 300 min was required to produce a sideband in the melt-spun alloy (Fig. 2(c)).

Comparing the quenched and melt-spun samples indicated that early stage spinodal decomposition was strongly affected by the initial conditions; namely, by the size of clusters introduced prior to aging. Differences in the initial states caused the differences

in the spinodal decomposition. Although the differences in initial states probably play important roles in the decomposition process (Fig. 12), the difference between the samples decreased with annealing time; thus the difference in the initial conditions affects early stage of decomposition process. In addition, as stated in Section 3.3, the presence of pure spinodal decomposition should be proved, assuming that the free energies of various phases in melt-spun samples are similar to that in Fig. 11.

In this work, we did not consider the As-Q conditions of the melt-spun samples in full. In the BF and DF images (Fig. 4), we did not observe clusters. Additionally, we could not verify the precise sizes of quenched and melt-spun samples experimentally by high-resolution TEM, XSAS, or neutron small-angle scattering. The initial clusters can be analyzed by atom probe field ion microscopy (APFIM). The relationships between the concentration [atom %] and depth [nm] of each component in Cu-Ti [32], Cu-Ni-Fe [33], and Fe-Cr-Co alloys [34] have been analyzed by APFIM. Furthermore, the 3D reconstruction of atom positions in a volume of  $15 \times 15 \times 18$  nm or  $14 \times 14 \times 30$  nm may be possible by the 3D-atom probe method (3D-AP) [35,36]. Therefore, quantitative estimations of the initial clusters for both types of samples will be possible. We intend to perform further studies using APFIM and 3D-AP to determining the precise cluster sizes in the early stages of spinodal decomposition.



## Figure Captions

- Fig. 1.** Diffraction profiles of melt-spun samples aged at 350 °C for 0 (As-Q), 20, 40, 60, 300, 600, and 1200 min.
- Fig. 2.** (200) diffraction profiles of melt-spun samples aged at 350 °C for 0 (As-Q), 20, 40, 60, 300, 600, and 1200 min. Magnifications of the profiles for the As-Q sample (a), and the samples aged at 350 °C for 60 (b), 300 (c), and 1200 min (d). The arrows indicate the sideband.
- Fig. 3.** Diffraction patterns of the fcc matrix, and DO<sub>22</sub>, and L<sub>12</sub> ordering reported by Zhao and Notis [12].
- Fig. 4.** TEM BF micrograph (a), TEM DF micrograph (b) and SADP (c) of the melt-spun sample aged for 0 min (As-Q) with an exposure time 0.1 s.
- Fig. 5.** TEM BF micrograph (a), enlarged view (a'), TEM DF micrograph (b), and SADP (c) of the melt-spun sample aged at 350 °C for 20 min with an exposure time of 1.0 s.
- Fig. 6** TEM BF micrograph (a), enlarged view (a'), TEM DF micrograph (b) and SADPs with an exposure time of 0.1 s (c) and 1.0 s (d) of the melt-spun sample aged at 350 °C for 40 min.
- Fig. 7.** TEM BF micrograph (a), enlarged view (a'), TEM DF micrograph (b), enlarged view (b') and SADPs with an exposure time of 0.1 s (c) and 1.0 s (d) of the melt-spun sample aged at 350 °C for 60 min.
- Fig. 8.** TEM BF micrograph (a) and SADP (b) of the melt-spun sample aged at 350 °C for 300 min with an exposure time 1.0 s.
- Fig. 9** TEM BF micrograph (a), enlarged view (a'), TEM DF micrograph (b), enlarged view (b'), and SADP with an exposure time 1.0 s (c) of the

melt-spun sample aged at 350 °C for 1200 min .

**Fig. 10.** Schematics of the differences in the initial states between quenched (a) and melt-spun samples (b).

**Fig. 11.** Schematic of the free energies as a function of the Sn component based on the results reported by Zhao and Notis [12], showing the relationships between the free energies of the disordered fcc ( $\alpha$  phase), DO<sub>22</sub>, L1<sub>2</sub>, and  $\gamma$ (DO<sub>3</sub>) phases.

**Fig. 12.** TTT diagram for the Cu-15Ni-8Sn alloy [12] and our experimental data for the melt-spun sample annealed at 350 °C.

## References

- [1] L.H.Schwartz, S.Mahajan, J.T.Plewes, Spinodal decomposition in a Cu-9 wt% Ni-6 wt% Sn alloy, *Acta. Metall.* 22(1974) 601-609.
- [2] L.H.Schwartz, J.T.Plewes, Spinodal decomposition in Cu-9wt% Ni-6wt% Sn—II. A critical examination of mechanical strength of spinodal alloys, *Acta Metall.* 22 (1974) 911-921.
- [3] J.T.Plewes, High-strength Cu-Ni-Sn alloys by thermomechanical processing, *Metall. Trans. A6* (1975) 537-544.
- [4] W.R.Cribb, J.O Ratka, Copper spinodal alloys, *Adv. Mater. Process.* 11g (2002) 27-30.
- [5] S-Z.Zhang, B-H.Jiang, W-J.Ding, Wear of Cu–15Ni–8Sn spinodal alloy, *Wear.* 264 (2008) 199-203.
- [6] F.M.Helmi, L.Zsoldos, On the thermal decomposition of Cu-Ni-Sn after prior cold-work, *Scr.Metall.* 11(1977)899-901.
- [7] P.Kratochvil, W.Biegel, B.Sprusil, B.Chalupa, Deformation and phase stability of Ni<sub>2</sub>CuSn intermetallic compound, *Phys.Status Solidi A* 131(1992)321-332.
- [8] H.Pal, S.K.Pradhan, M.De, Microstructure and phase-transformation studies of Cu-Ni-Sn alloys, *Jpn. J. Appl. Phys.* 34 (1995) 1619-1626.
- [9] S.Kondo, A.Masusaki, K.Ogawa, T.Morimura, H.Nakashima, Effect of initial states on the spinodal decomposition of quenched and melt-spun Cu-15Ni-8Sn alloy, *Mater.Trans.* 56 (2015) 23-29.
- [10] E.G.Baburaj, U.D.Kulkarni, E.S.K.Menon, R.Krishnan, Initial stages of decomposition in Cu-9Ni-6Sn, *J.Appl.Crystallogr.* 12 (1979) 476-480.

- [11] P.Kratochvil, J.Mencl, J.Pešićka, S.N.Komnik, The structure and low temperature strength of the age hardened Cu-Ni-Sn alloys, *Acta Metall.* 32 (1984) 1493-1497.
- [12] J.-C. Zhao, M.R. Notis, Spinodal decomposition, ordering transformation, and discontinuous precipitation in a Cu-15Ni-8Sn alloy, *Acta. Mater.* 46 (1998) 4203-4218.
- [13] Ph.Goudeau, A.Naudon, Anomalous small-angle X-ray scattering study of the early stages of decomposition in Cu-15wt%Ni-8wt%Sn, *J.Appl.Crystallogr.* 23 (1990) 266-276.
- [14] L.H.Schwartz, S.Mahajan, J.T.Plewes, Spinodal decomposition in a Cu-9 wt% Ni-6 wt% Sn alloy, *Acta Metall.* 22 (1974) 601-609.
- [15] B.Ditchek, L.H.Schwartz, Diffraction study of spinodal decomposition in Cu-10 w/o Ni-6 w/o Sn, *Acta.Matall.* 28(1980) 807-822.
- [16] H.Sagane, N.Kuwano, K.Oki, X-ray side bands analysis on modulated structure evolution in Cu-Ni-Sn Alloy, *J.Japan Inst Metals.* 56 (1992) 998.
- [17] L.E.Collins, J.R.Barry, Reduced segregation in rapidly solidified Cu-Ni-Sn alloys, *Mater.Sci.Eng.* 98 (1988) 335-338.
- [18] M.Miki, Y.Ogino, Precipitation in a Cu-20%Ni-8%Sn alloy and the phase diagram of the Cu-Ni Rich Cu-Ni-Sn system, *Mater.Trans.* 25 (1984) 593-602.
- [19] H.Miyake, A.Furusawa, T.Ariyasu, A.Okada, Optical measurement of cooling rate during splat cooling process, *Imono*, 66 (1994) 734-738.
- [20] W.A.Soffa, D.E.Laughlin, High-strength age hardening copper-titanium alloys: redivivus, *Prog.Mat.Sci.* 49 (2004) 347-366.
- [21] I.S.Batra, G.K.Dey, U.D.Kulkarni, S.Banerjee, On the sequence of clustering and ordering in a meltspun Cu-Ti alloy, *Mat.Sci.Eng.A360* (2003) 220-227.

- [22] F. Findik, Sidebands in spinodal Cu-Ni-Cr alloys and lattice parameters inquiries, *J. Mater. Sci. Lett.* 12 (1993) 338-342.
- [23] V.M. López-Hirata, Á.D.J. Arias-Pérez, M.L. Saucedo-Muñoz, A study of precipitation in a Cu-15 wt%Ni-8 wt%Sn alloy, *J. Mater. Sci. Lett.* 18 (1999) 1697-1699.
- [24] P. Sahu, S.K. Pradhan, M. De, X-ray diffraction studies of the decomposition and microstructural characterization of cold-worked powders of Cu-15Ni-Sn alloys by Rietveld analysis, *J. Alloy. Comp.* 377 (2004) 103-116.
- [25] F. Izumi, K. Momma, Three-Dimensional Visualization in Powder Diffraction, *Solid State Phenom.* 130 (2007) 15-20.
- [26] V. Daniel, H. Lipson, An X-Ray study of the dissociation of an alloy of copper, iron and nickel, *Proc. Roy. Soc. Lond. A* 181 (1943) 368-378.
- [27] V. Ganesan, K.S. Raghavan, Expressions for spinodal wavelength in orthorhombic and tetragonal structure systems, *J. Mat. Sci. Lett.* 15 (1996) 1471-1474.
- [28] L.D. Wang, C.L. Chen, M.K. Kong, On the daniel-lipson's wavelength formula of spinodal decomposition, Y.H. Wei, *Scr. Mater.* 42 (2000) 725-730.
- [29] W.A. Soffa, D.E. Laughlin, *Proc. Int. Conf. Solid-Solid Transformations* ( TMS, Warrendale, Pennsylvania, 1982) p.159.
- [30] D.E. Laughlin, W.A. Soffa, , *Physical Properties and Thermodynamic Behaviour of Minerals* ( NATO ASI Series C, Vol.225, 1988) p.213.
- [31] W.A. Soffa, D.E. Laughlin, Decomposition and ordering processes involving thermodynamically first-order order  $\rightarrow$  disorder transformations, *Acta metall.* 37 (1989) 3019-3028.

- [32] L.V.Alvensleben,R. Wagner, *Decomposition of Alloys : the early stages*  
( Pergamon,NewYork,1984), p143
- [33] J.Piller, W.Wagner, H.Wollenberger,P.Mertens, *Decomposition of Alloys : the early stages* ( Pergamon,NewYork,1984), p156
- [34] W.A.Soffa, S.S.Brenner,M.KMiller, *Decomposition of Alloys : the early stages*  
( Pergamon,NewYork,1984), p227
- [35] M. Murayama, K. Hono, Y. Katayama, Microstructural evolution in a 17-4 PH stainless steel after aging at 400 °C, Met. Mater. Trans. A. 30(1999)345-353.
- [36] A. Manzoni, H. Daoud, S. Mondal, S.vanSmaalen, R. Völkl, U. Glatzel, N. Wanderka, Investigation of phases in  $\text{Al}_{23}\text{Co}_{15}\text{Cr}_{23}\text{Cu}_8\text{Fe}_{15}\text{Ni}_{16}$  and  $\text{Al}_8\text{Co}_{17}\text{Cr}_{17}\text{Cu}_8\text{Fe}_{17}\text{Ni}_{33}$  high entropy alloys and comparison with equilibrium phases predicted by Thermo-Calc, J. Alloy. Comp. 552 (2013) 430-436.

Table 1      Relative X-ray intensities of the (200) peak for the melt-spun samples annealed at 350 °C for 0 (As-Q), 20, 40, 60, 300, 600, and 1200 min, with the intensity of the (111) peak set as 1.

Table 1

	(111)	(200)
AsQ	1	1.05
350°C 20min	1	1.09
350°C 40min	1	1.04
350°C 60min	1	0.82
350°C 300min	1	0.75
350°C 600min	1	0.75
350°C 1200min	1	0.75

Table 2      Lattice parameter  $a$  of the melt-spun samples annealed at 350 °C for 0 (As-Q), 20, 40, 60, 300, 600, and 1200 min.

Table 2

	$a$ /nm
AsQ	0.3648
350°C 20min	0.3651
350°C 40min	0.3647
350°C 60min	0.3649
350°C 300min	0.3650
350°C 600min	0.3643
350°C 1200min	0.3651

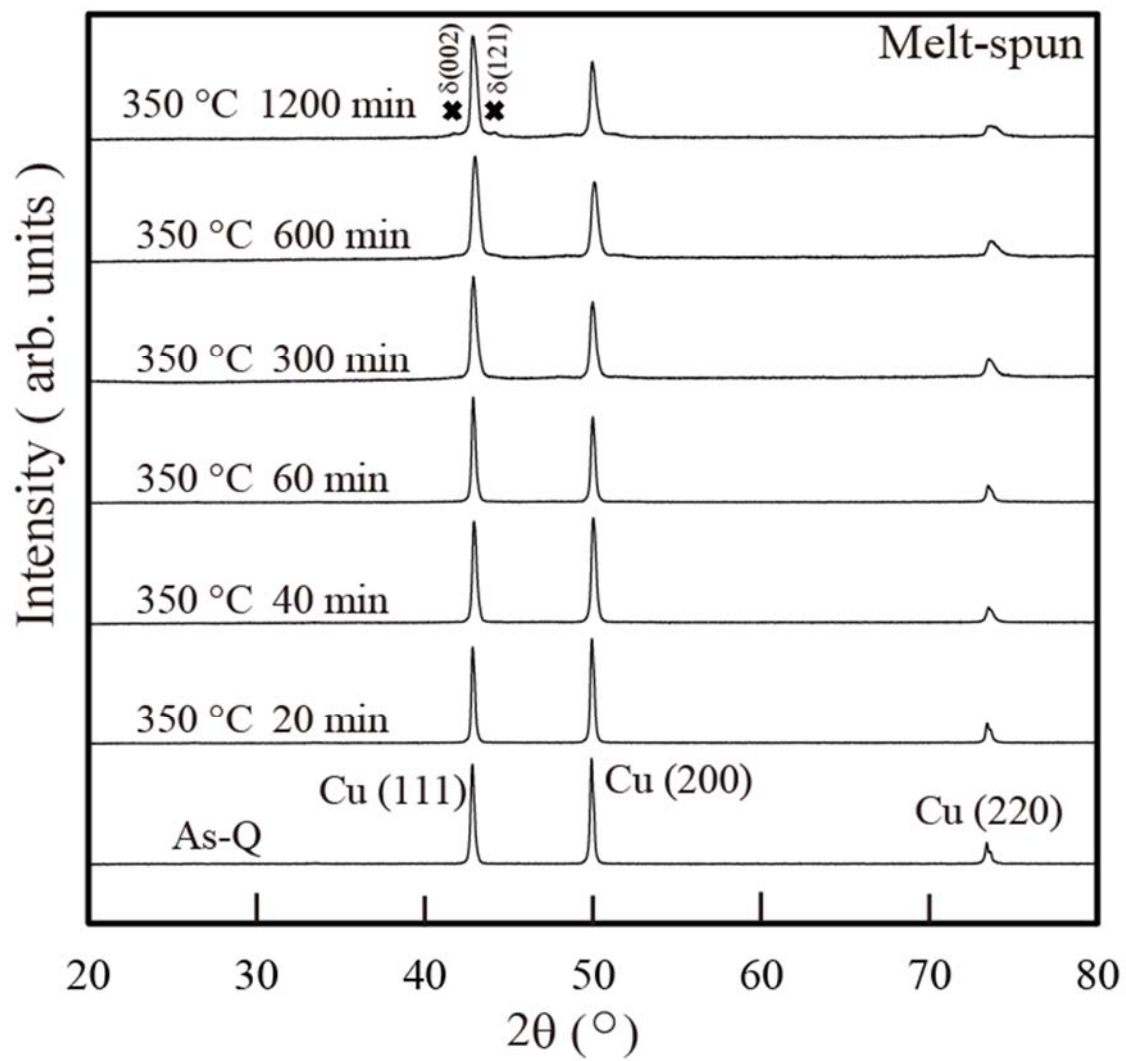


Fig.1



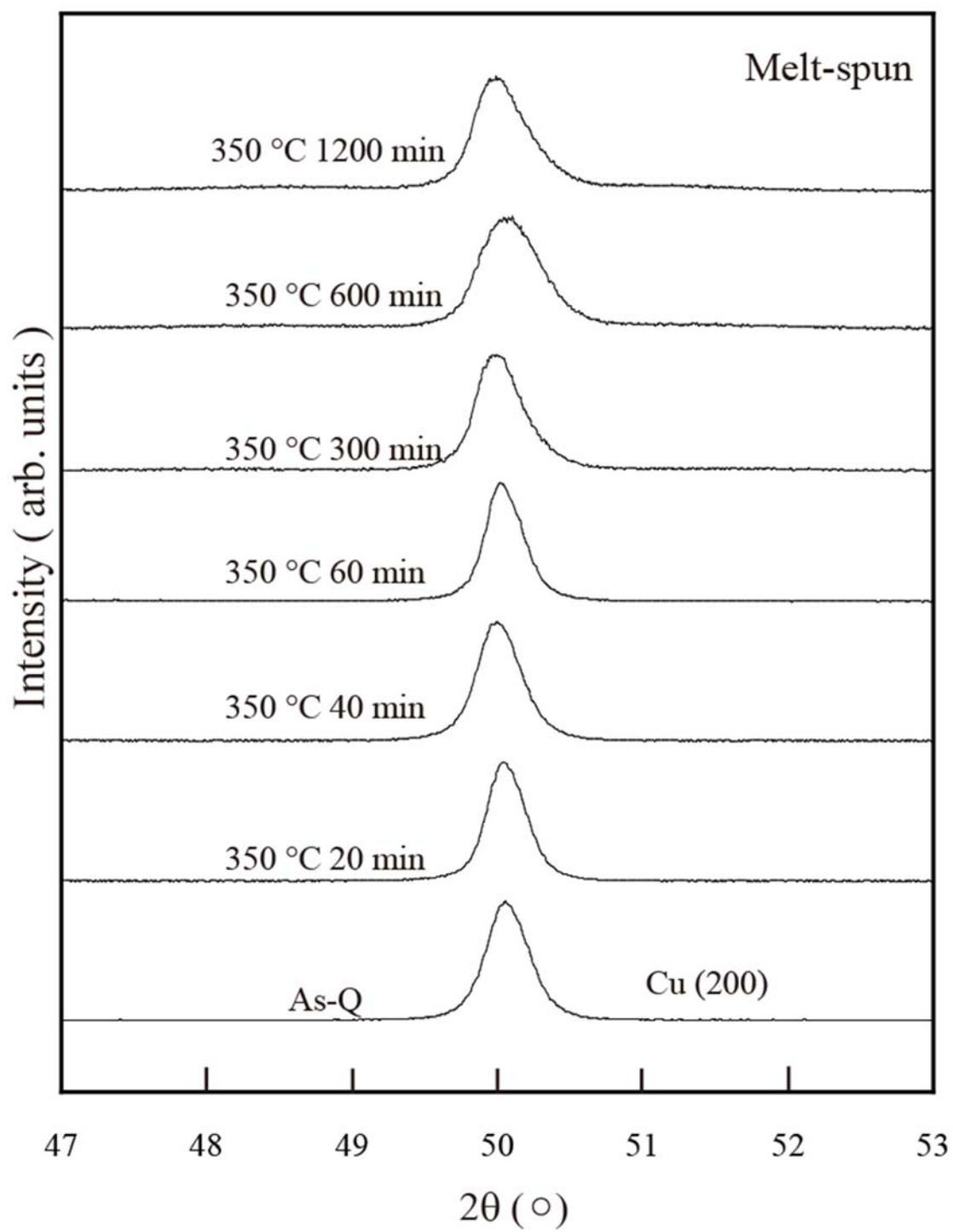


Fig.2

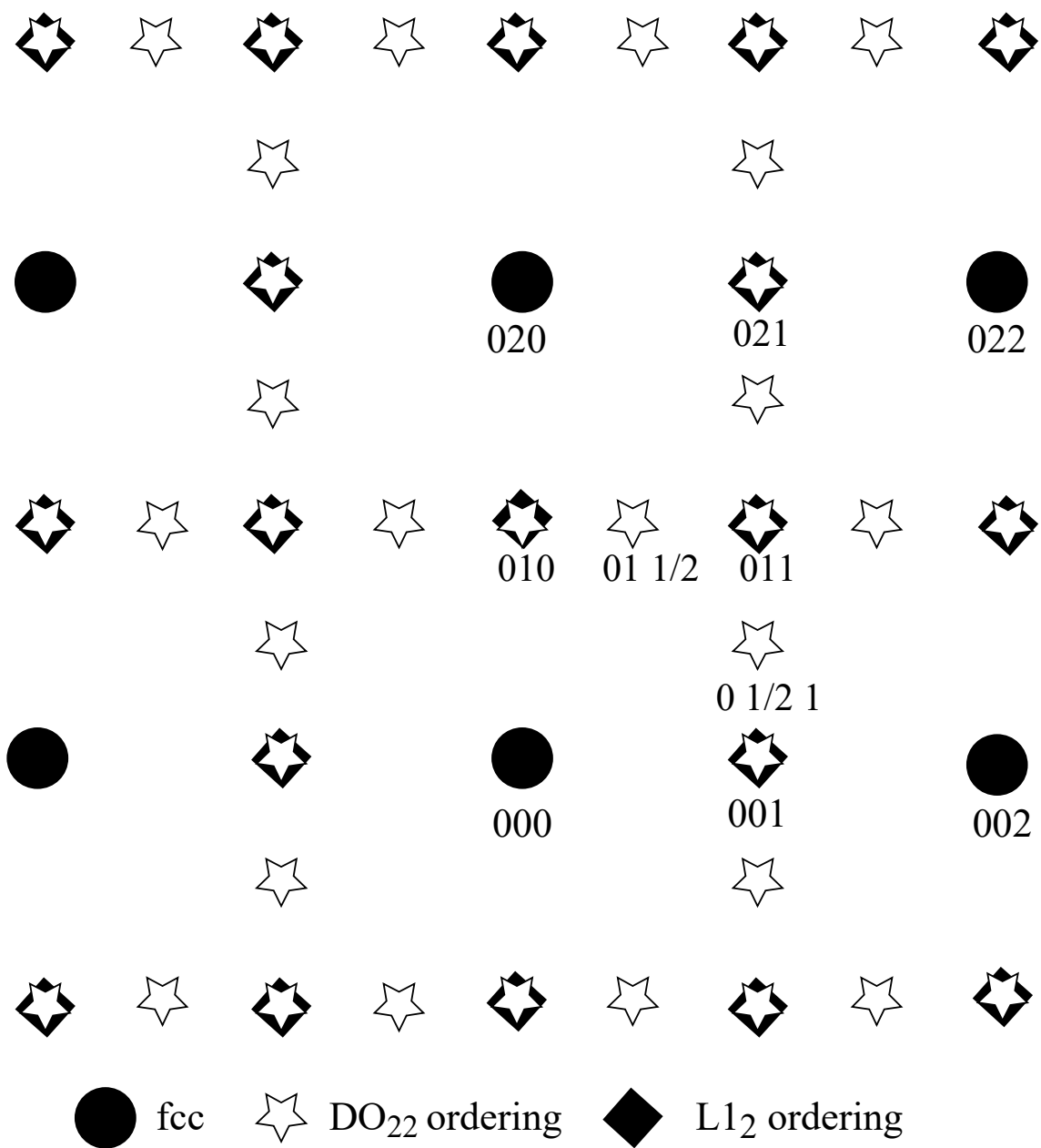


Fig. 3

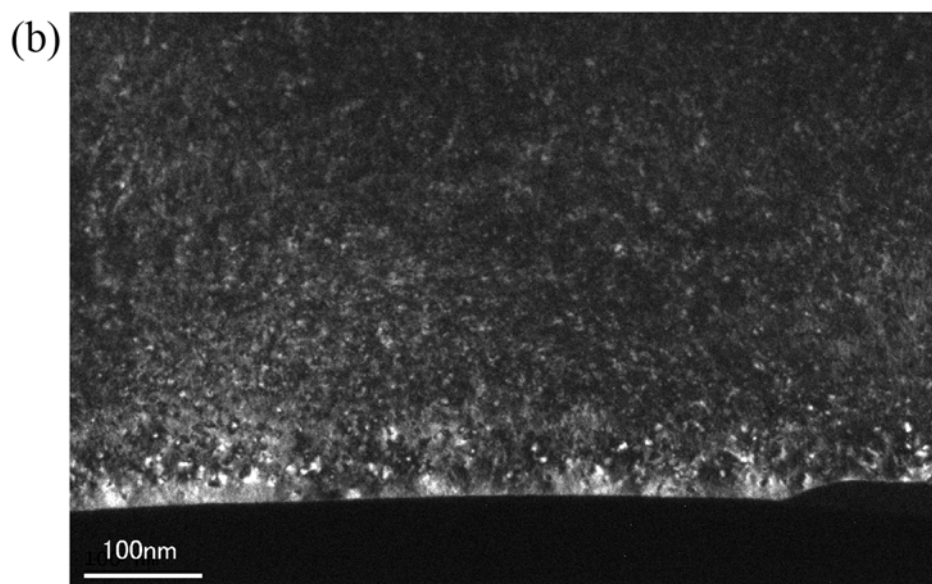
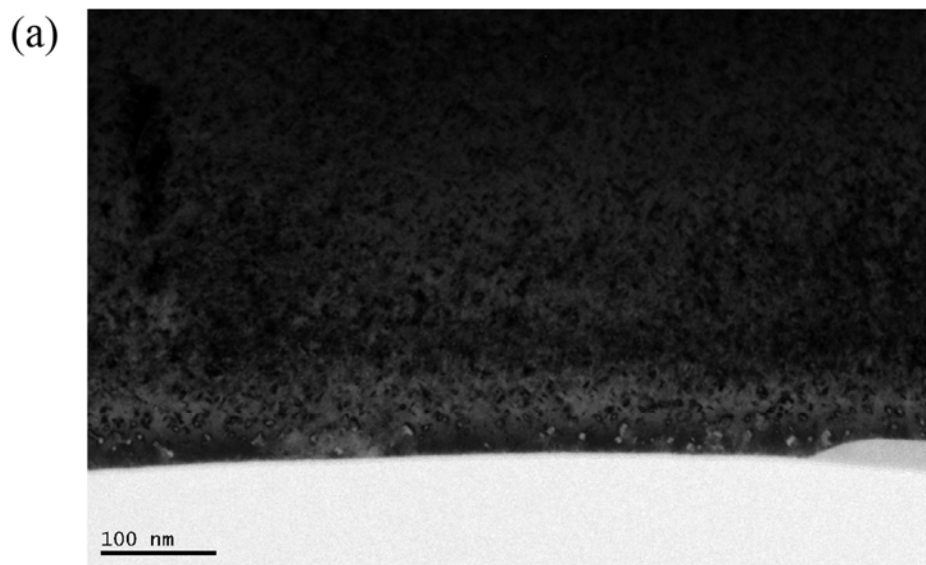


Fig.4

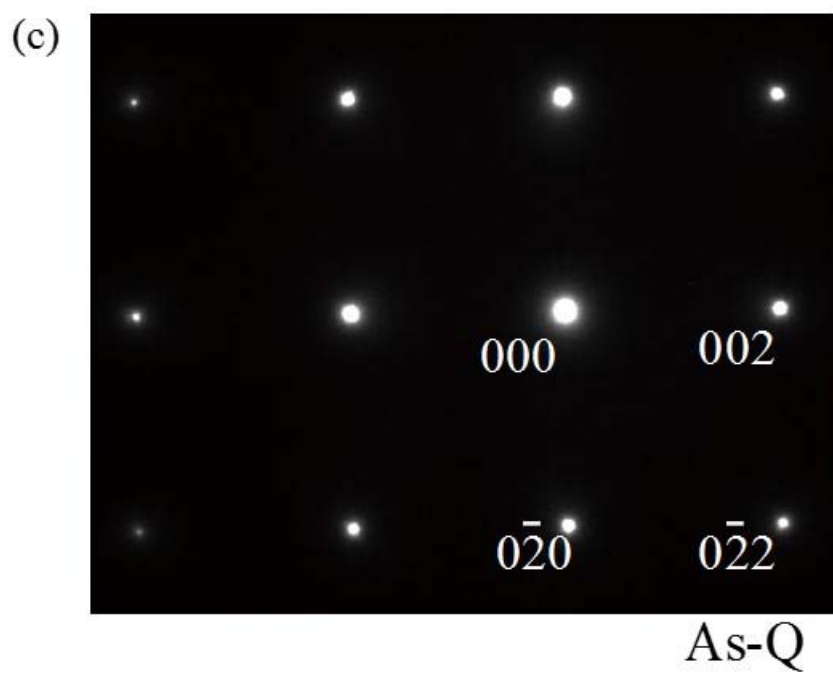


Fig.4

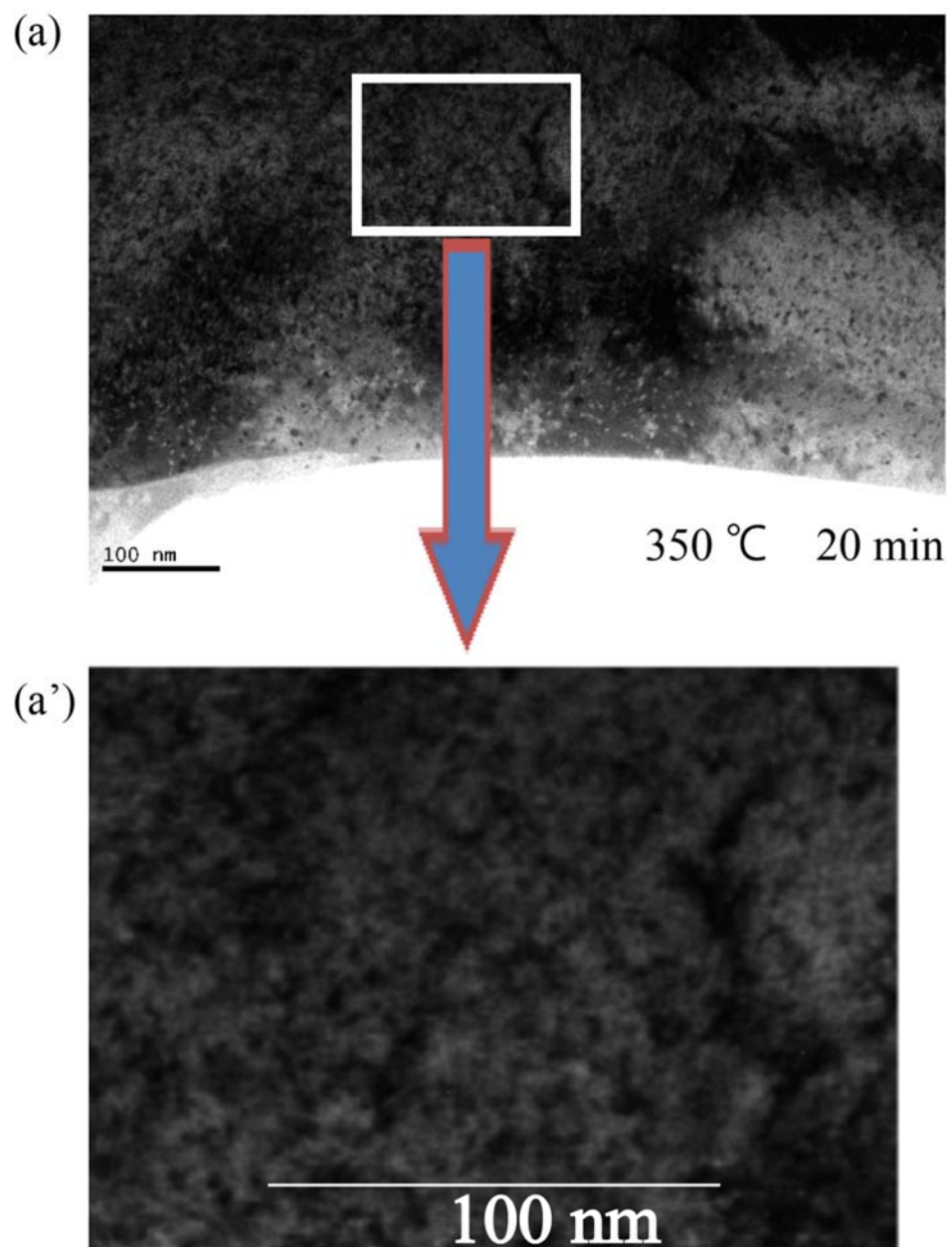


Fig.5

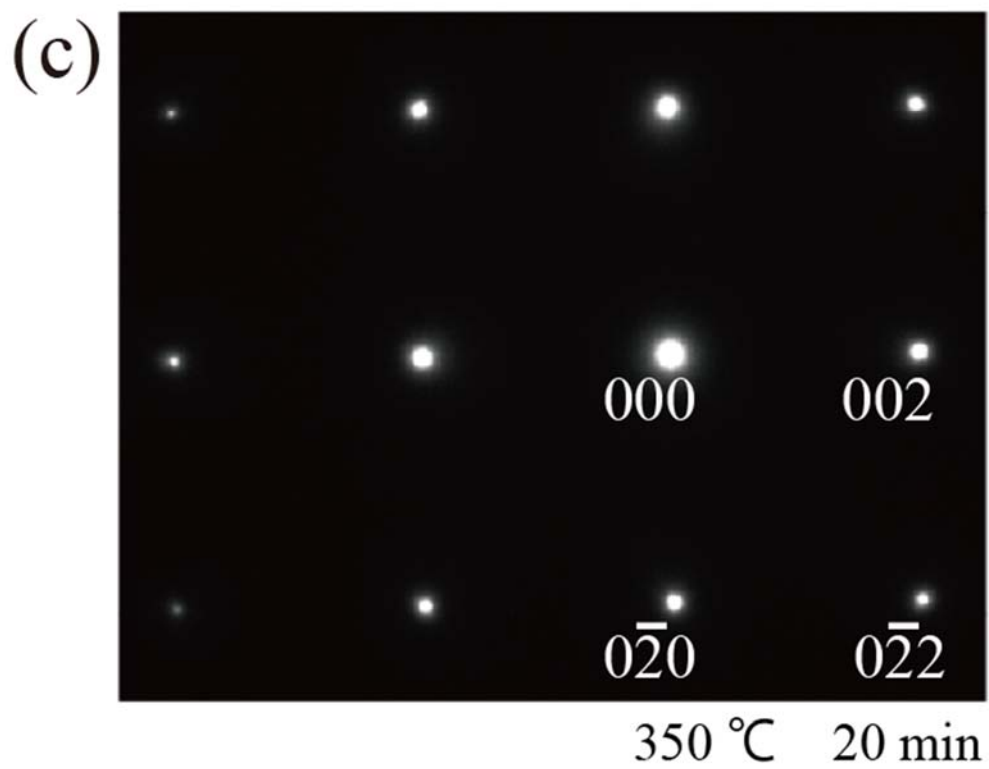
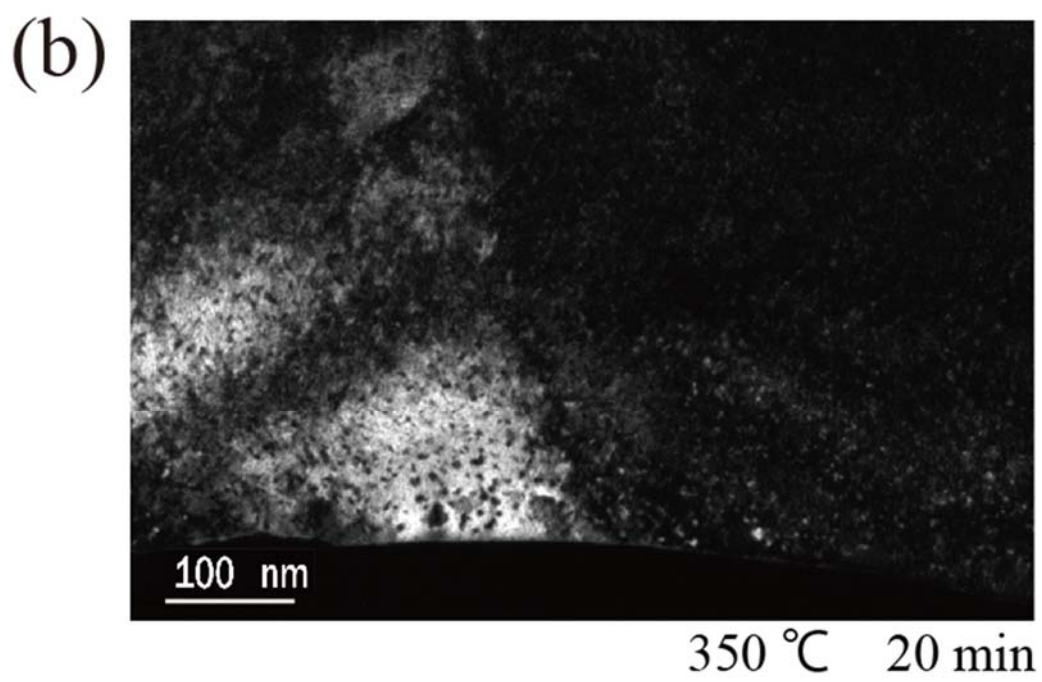


Fig.5

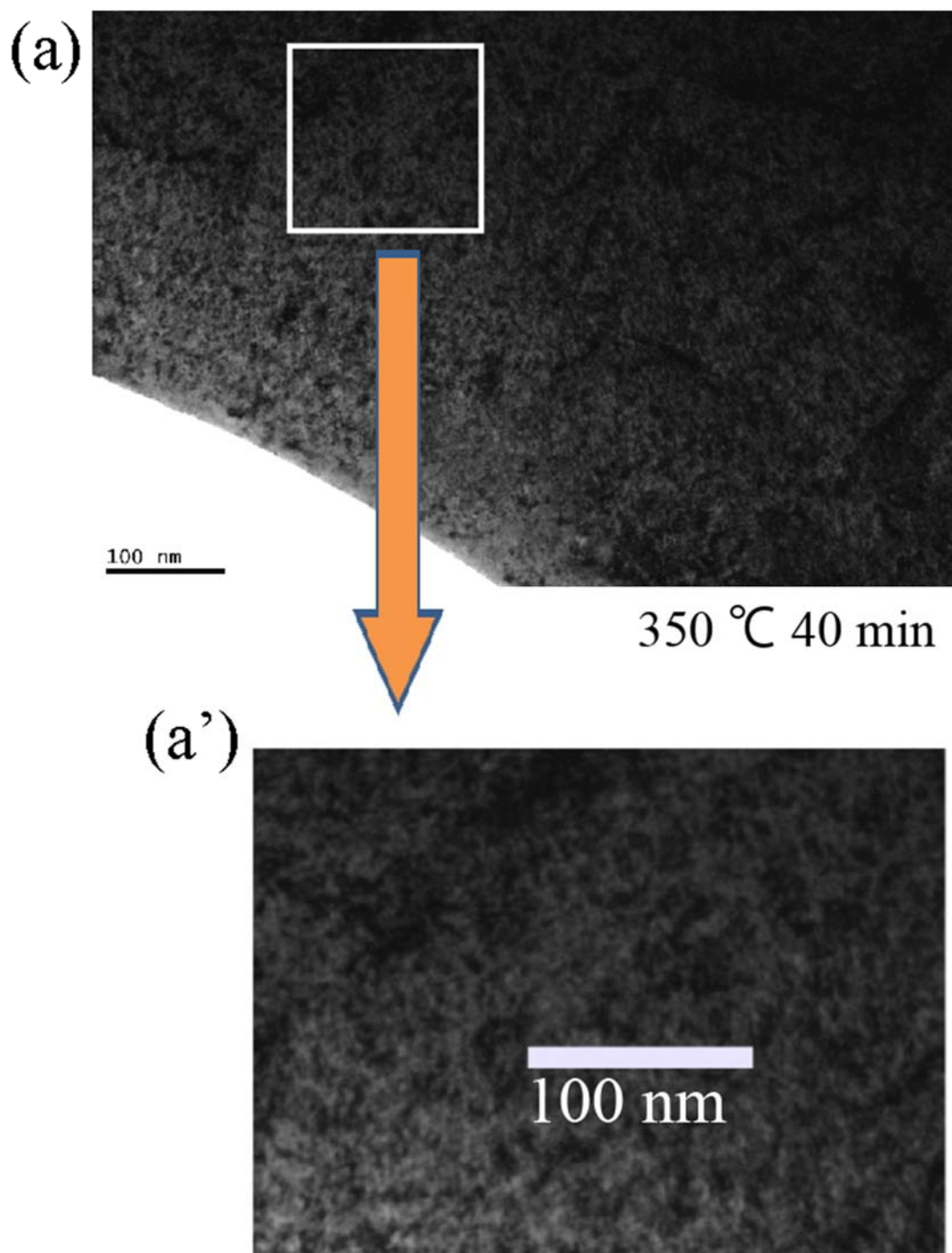


Fig.6

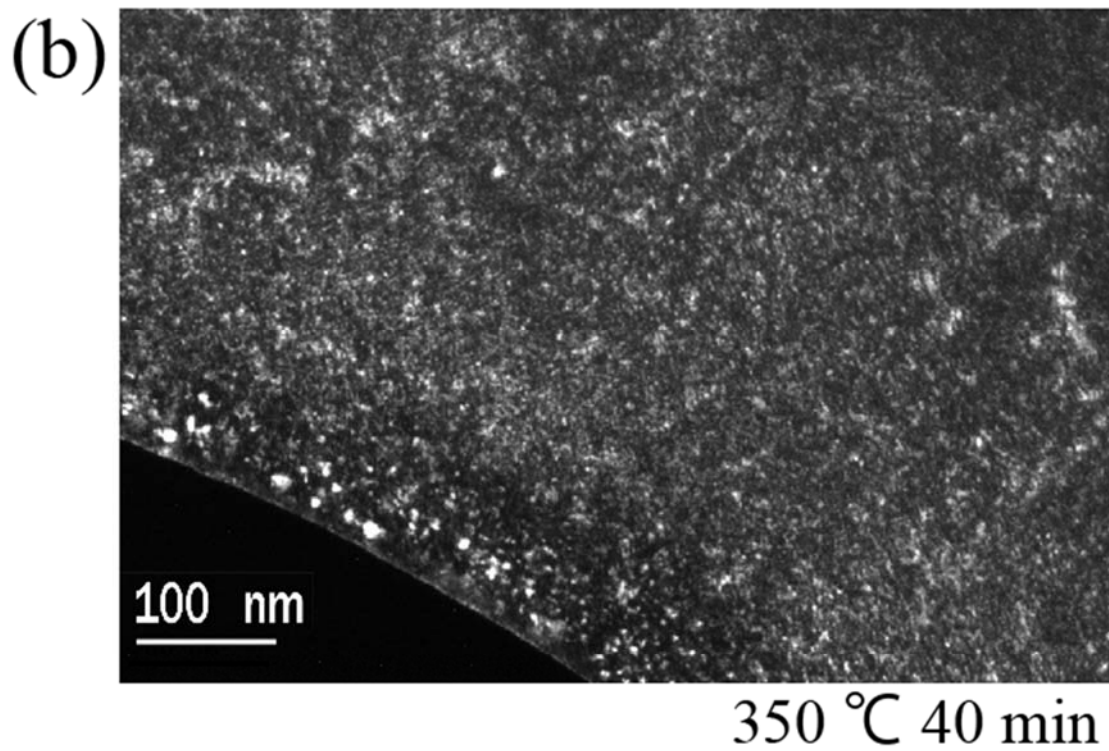


Fig.6



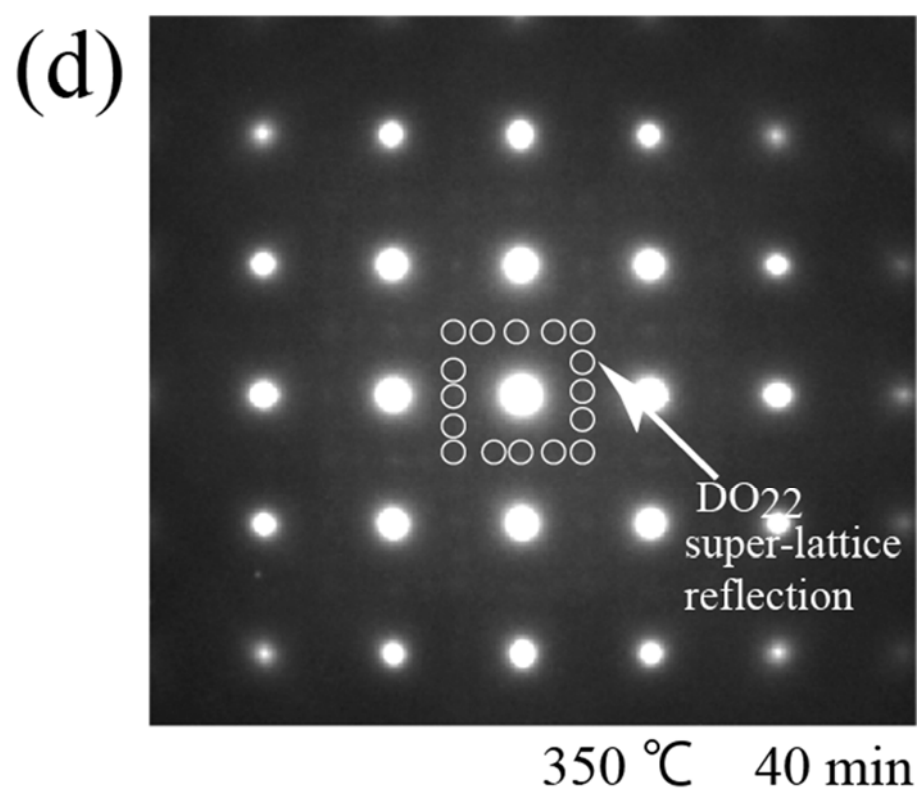
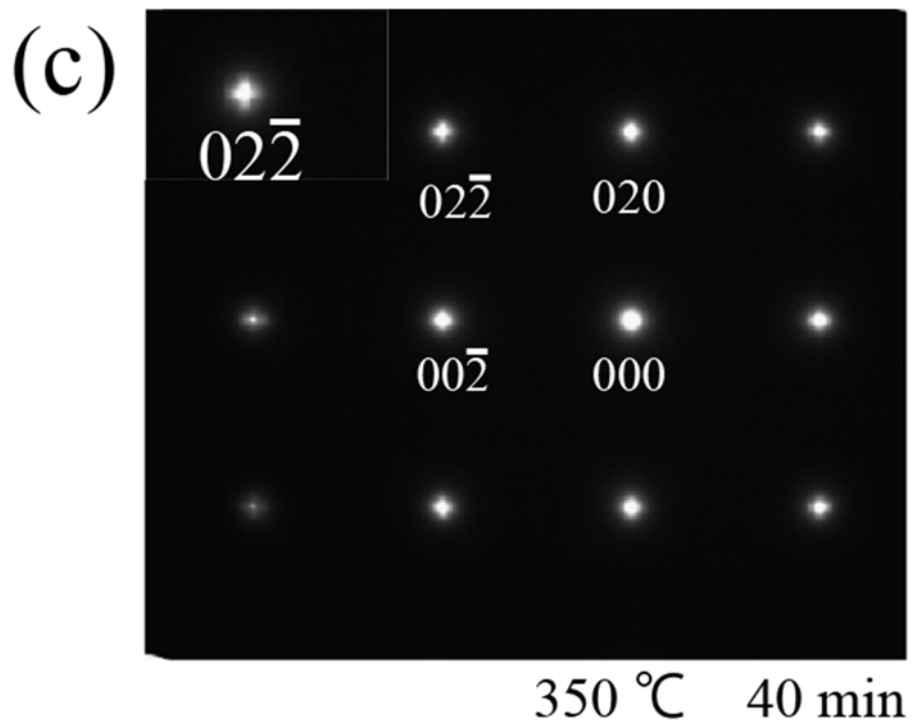


Fig.6

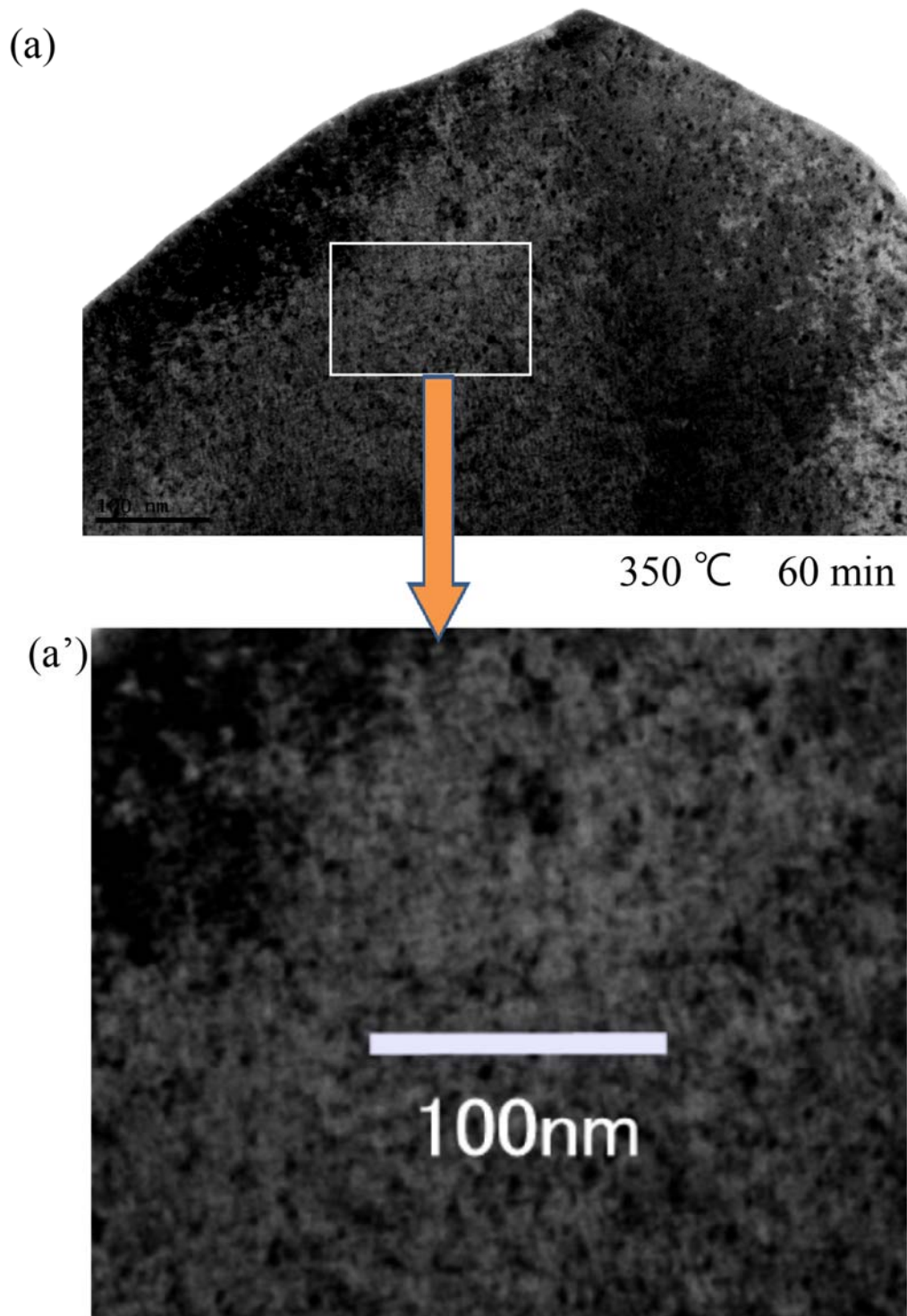


Fig.7

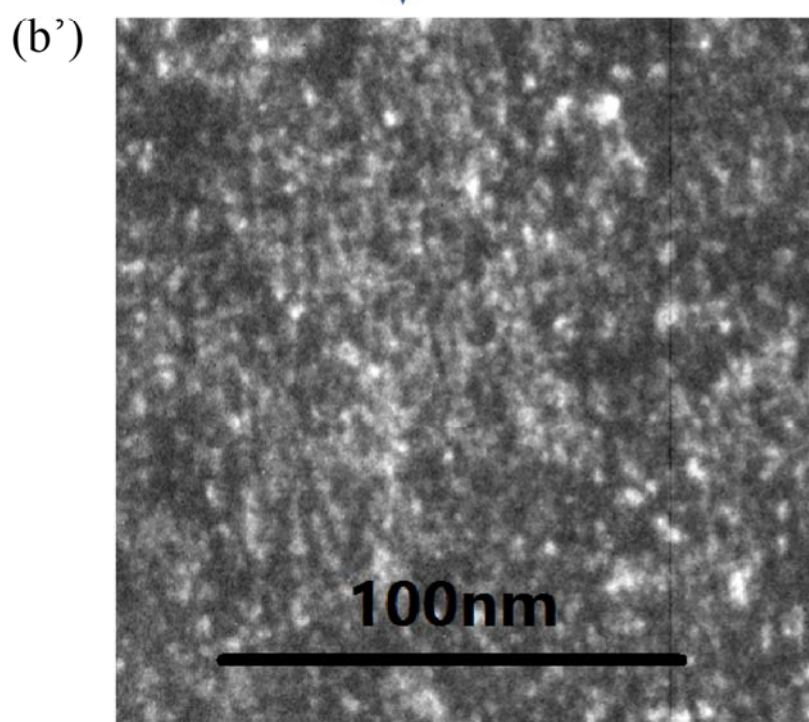
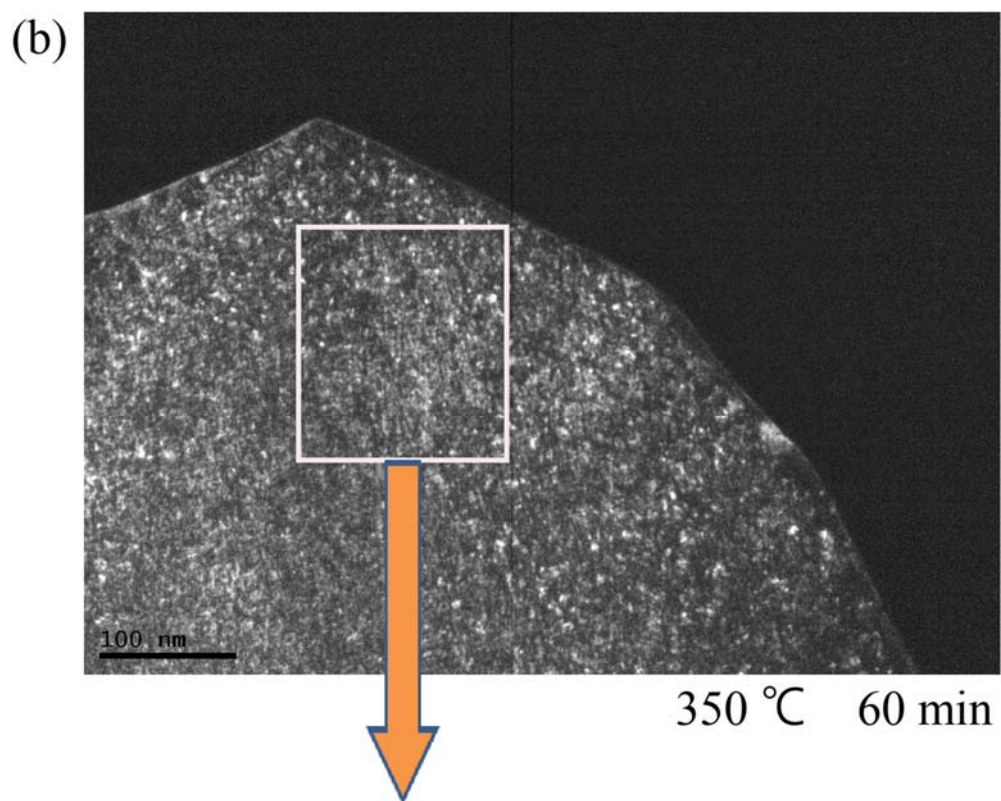


Fig.7

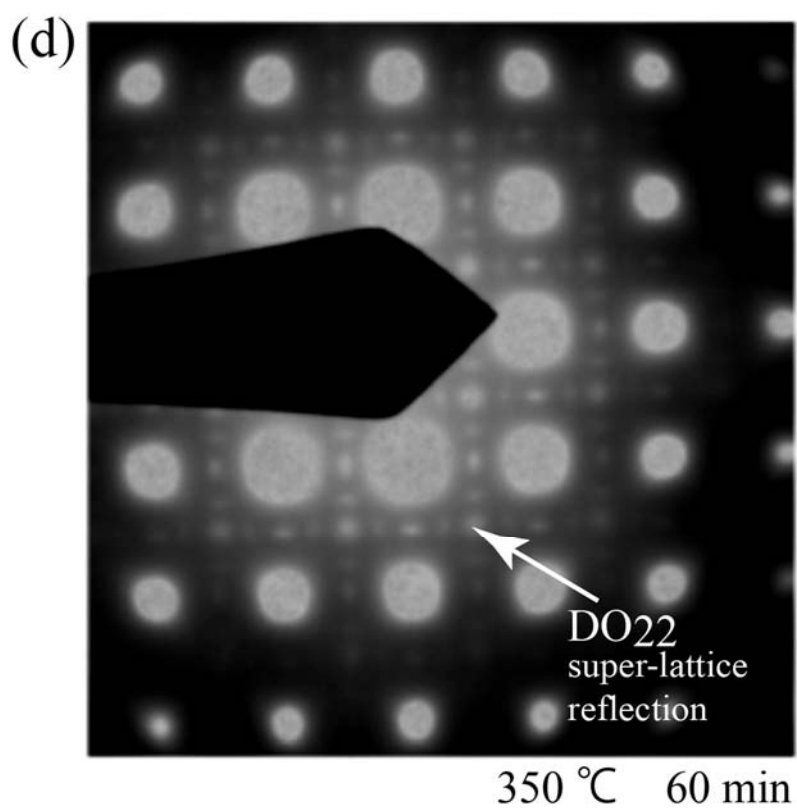
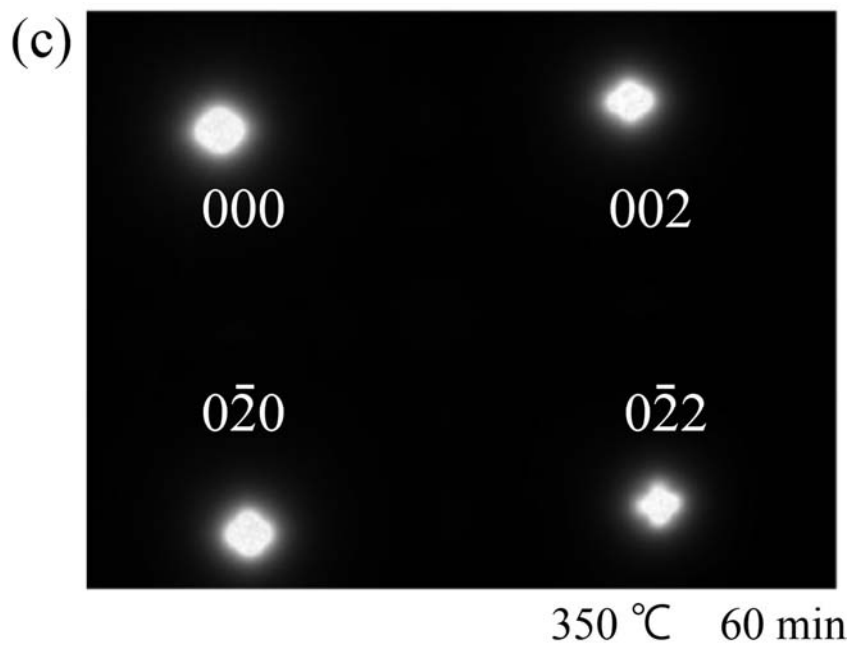


Fig.7

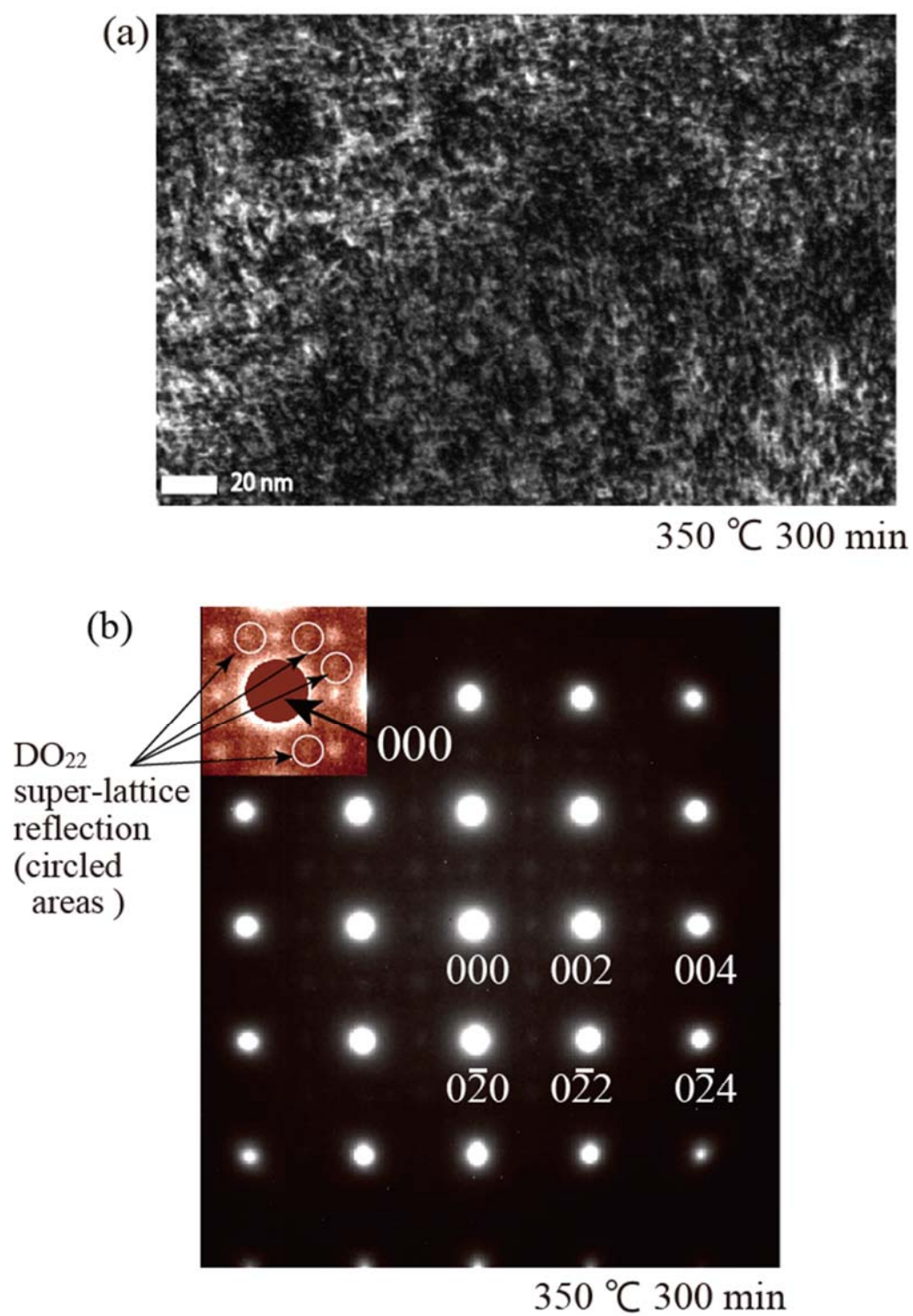


Fig.8

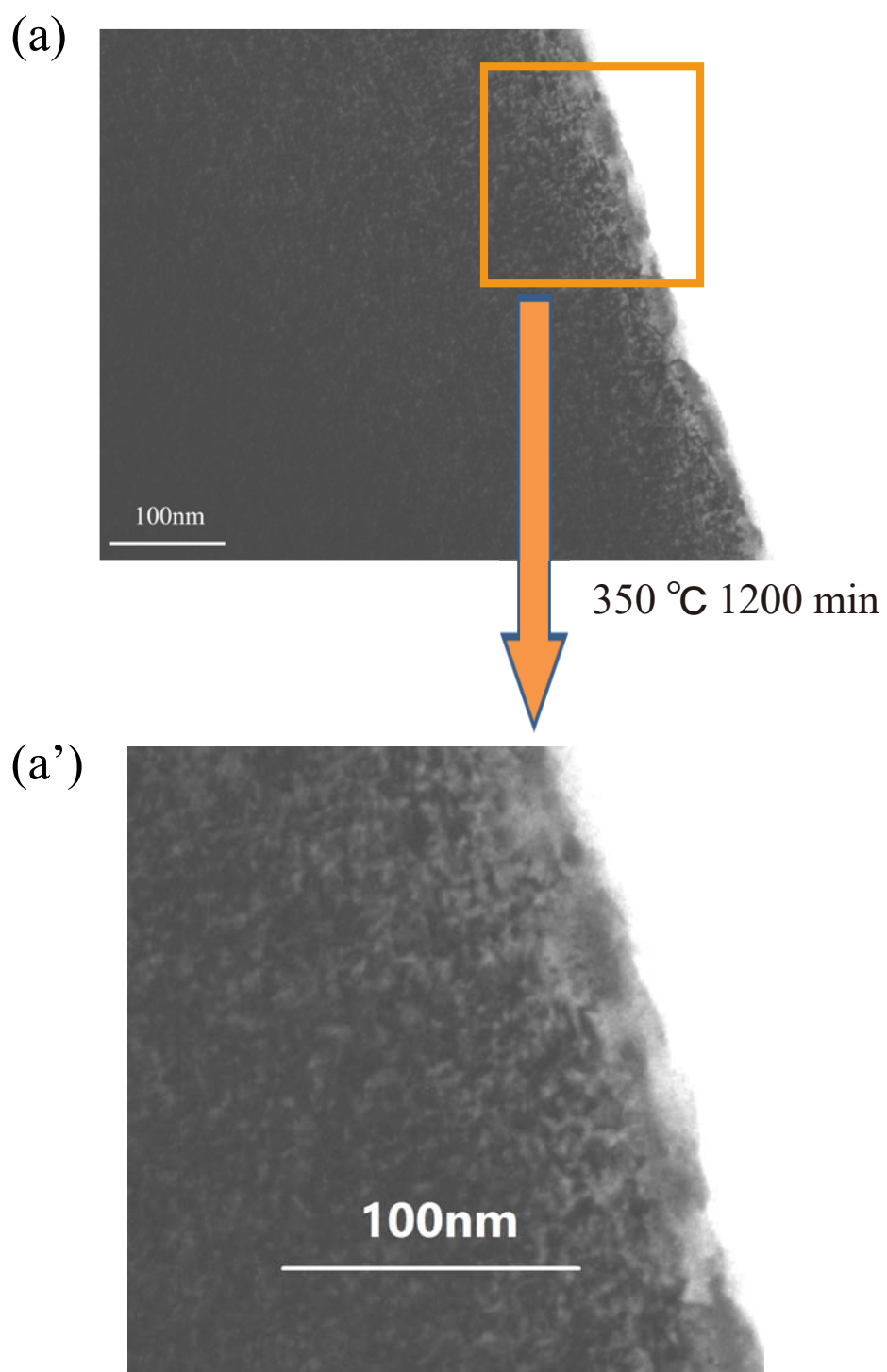


Fig.9



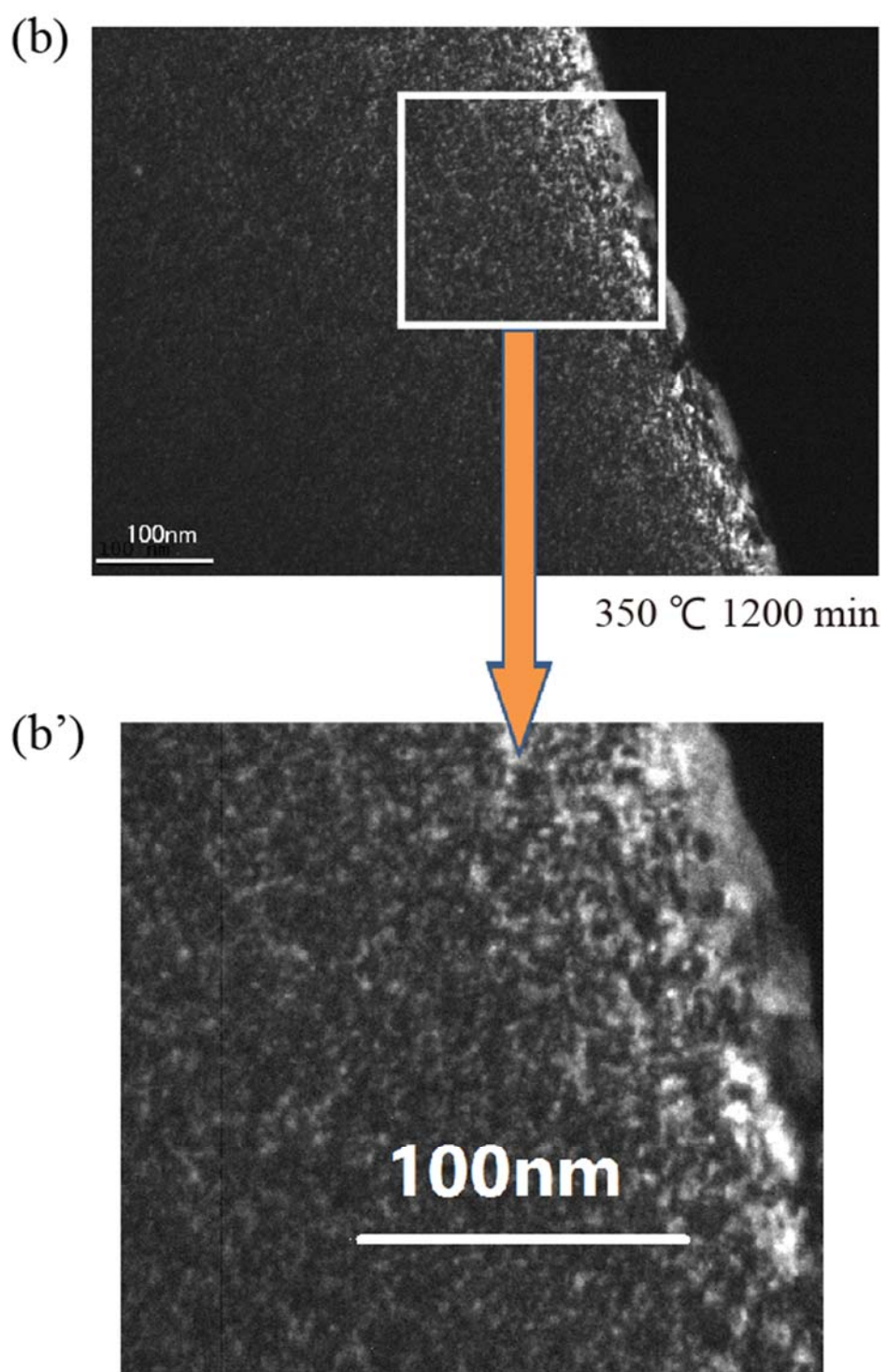


Fig.9

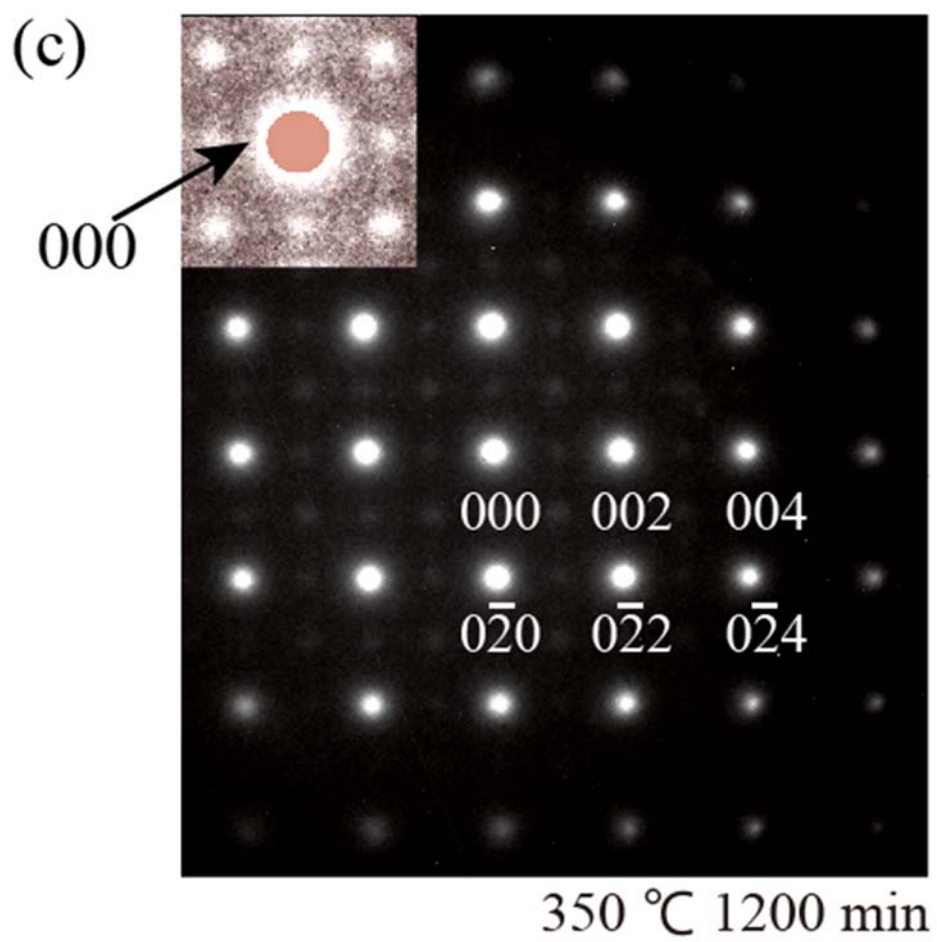


Fig.9



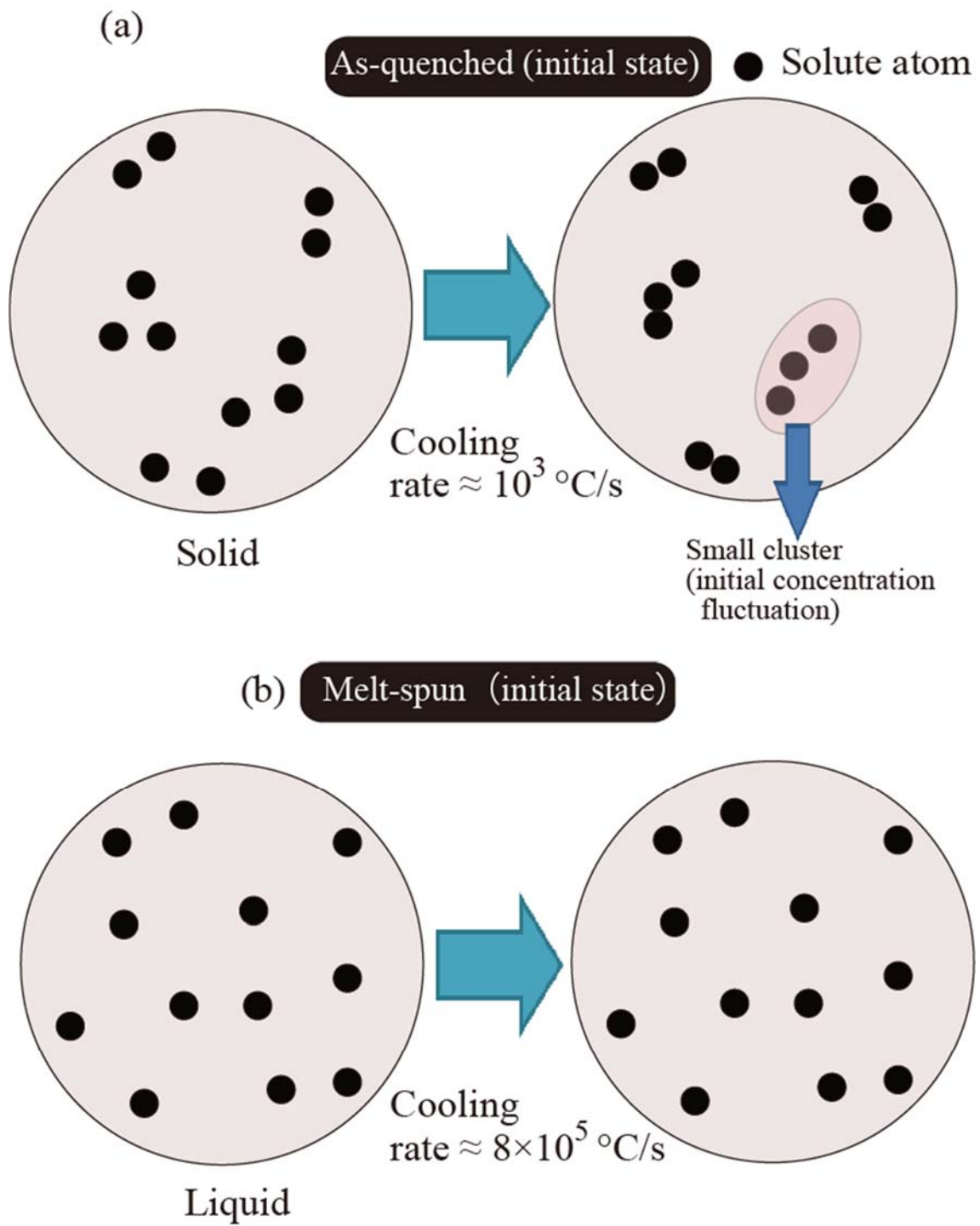


Fig.10

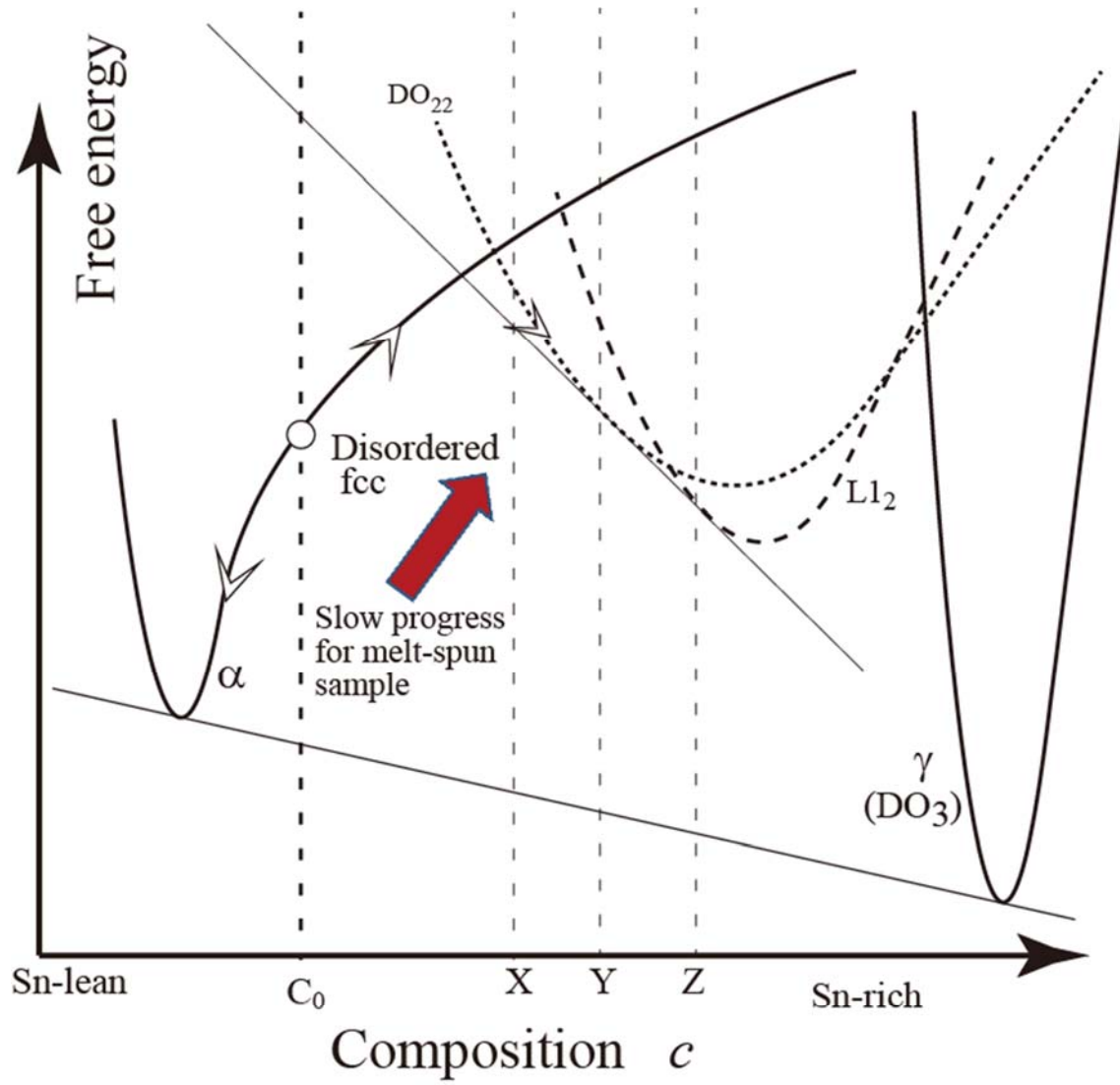


Fig.11

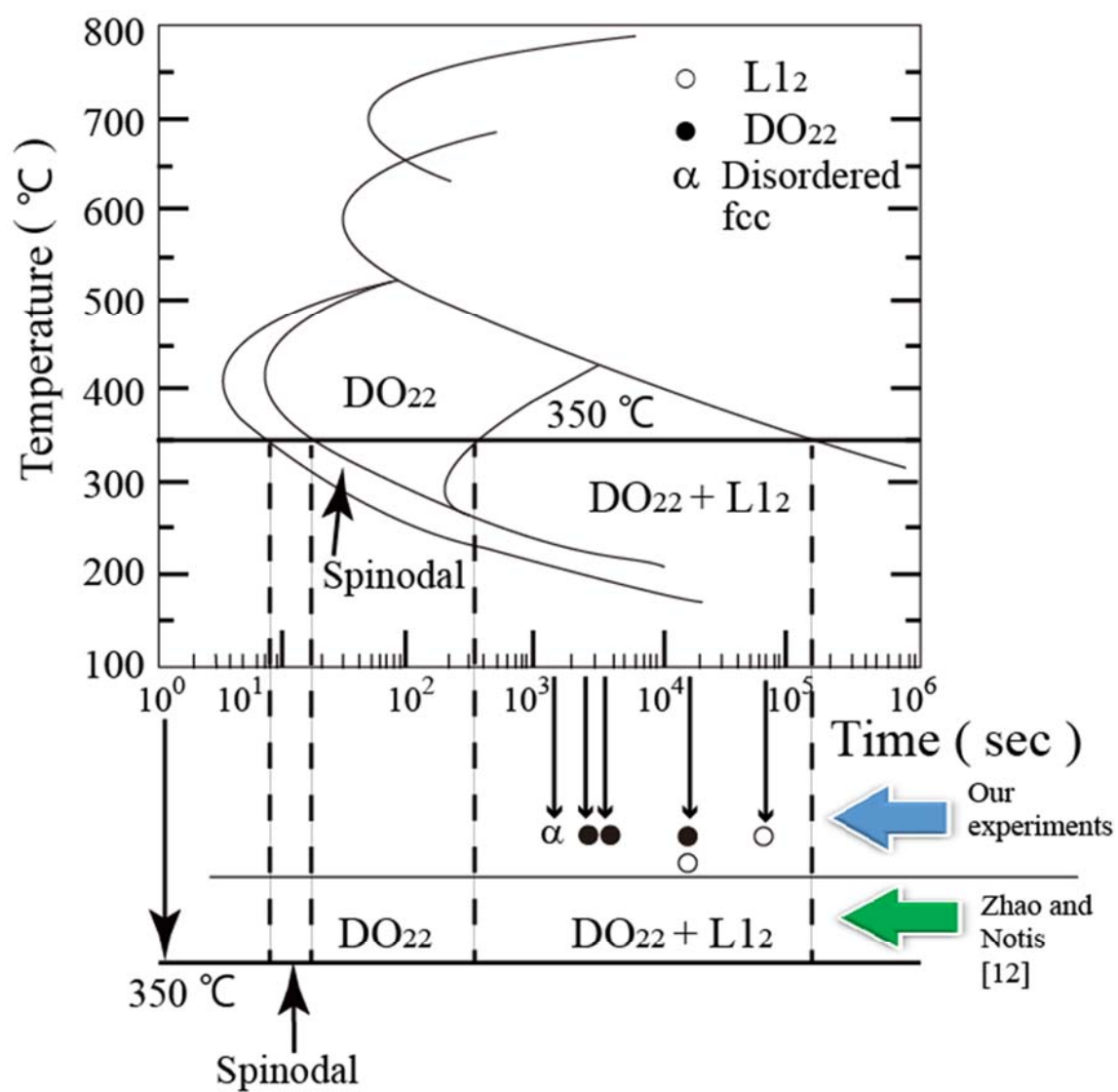


Fig.12